submitted to *Geophys. J. Int.*

First-order Control Factors for Ocean-bottom Ambient Seismology Interferometric Observations

Adesh Pandey[1], Jeffrey Shragge[1], Aaron J. Girard[1]

[1] *Center for Wave Phenomena, Department of Geophysics, Colorado School of Mines, Golden CO* 80401*, USA*

SUMMARY

Expanding the lower-frequency band of seismic energy sources, particularly below 2.0 Hz, is crucial for improving the stability and effectiveness of full waveform inversion (FWI). Conventional active sources including airguns are ineffective at generating low-frequency wavefields, while ambient seismic wavefields, driven by natural energy sources such as ocean waves, offer a promising alternative. Effectively using ambient wavefield energy for seismic imaging or inversion analyses, though, requires understanding key physical control factors contributing to observations - including ambient source mechanisms and distribution, ocean-bottom bathymetry, and Earth model heterogeneity - which influence wave-mode excitation and partitioning, particularly in the context of ocean-bottom ambient seismology interferometry. This study presents a modelling framework for simulating cross-correlation wavefields generated by ambient seismic sources for dense ocean-bottom sensor arrays within a coupled acoustic-elastic system, without relying on Green's function retrieval assumptions. We model velocity and pressure cross-correlation wavefields to explore the effects of ocean-bottom velocity structure, ambient source distributions, and bathymetric variations on seismic wave excitation and propagation in the low (0.01-2.00 Hz) frequency band. Our results show that the distribution of ambient energy source locations, whether at the seabed or sea surface, significantly affects excited wave-mode characteristics. Love waves are particularly evident in the presence of substantial lateral and vertical bathymetric variations and heterogeneous Earth structure. The distribution of azimuthal ambient energy sources also influences Love-wave excitation, with the most prominent waves observed in the direction of the highest source concentration. Additionally, not all virtual shot-gather components provide unique insights into wave-mode excitation and partitioning. This work improves the understanding of low-frequency ambient seismic wavefields in ocean environments, with potential applications in long-wavelength structural imaging and elastic velocity model estimation from FWI analysis.

Key words: Seismic interferometry; Seismic noise; Surface waves and free oscillations; Wave propagation

1 INTRODUCTION

Recent advancements in multi-component ocean-bottom sensor array deployments — including ocean-bottom seismometers (OBSs), cables (OBCs), and nodes (OBNs) — offer a unique opportunity for investigating marine ambient wavefield phenomena. When deployed in sparse (4-16 stations per km^2), large-scale ($>$ 100 km^2) arrays on the seafloor, these instruments enable the extraction and analysis of low-frequency (sub-2.0 Hz) wavefield information. Although primarily designed for active-source seismic exploration, continuous ocean-bottom recordings spanning one to three months often capture extensive data below the typical 2.0 Hz low-frequency cutoff of marine air-gun sources, often extending into the range beneath the noise floor of the receivers themselves. Traditionally considered ‘noise’, these seismic data — primarily originating from ambient seismic sources such as ocean swell noise (Longuet-Higgins 1950) — increasingly are being recognised for their potential to provide valuable surface-wave information through ambient seismic interferometry analyses.

As illustrative examples, ambient virtual shot gathers (VSGs) derived from OBN recordings in the Astero field offshore Norway yielded Scholte-wave group velocity images at frequencies between 0.18-0.40 Hz, correlating well with known subsurface structures (Bussat & Kugler 2011). Similarly, permanently deployed OBC arrays at the Valhall field in the Norwegian North Sea facilitated near-surface imaging through Scholte-wave group and phase velocities in the 0.50–1.75 Hz frequency range using straight-ray tomography (de Ridder & Dellinger 2011; de Ridder & Biondi 2013; Mordret et al. 2013). In the Gulf of Mexico, VSGs from continuous OBN array recordings revealed dispersive surface- and guided P-wave modes within the sub-2.0 Hz frequency band (Stewart 2006; Girard et al. 2023, 2024). Ning et al. (2024) used dispersion estimates derived from VSG observations from a sparse Gulf of Mexico OBN array for Scholte-wave inversion. The resulting shear-wave velocity (v_s) model, estimated to 3.0 km depth, exhibited structural similarity to the compressional-wave velocity (v_p) model obtained from full-waveform inversion (FWI) analysis of active-source seismic OBN data. These studies collectively demonstrate the potential of using the low-frequency information recorded in ocean-bottom sensor data for subsurface investigation, complementing conventional seismic exploration analysis.

In FWI analyses, low-frequency seismic data play a crucial role in effectively reducing cycle skipping, leading to faster convergence and stability in FWI (Virieux & Operto 2009). However, obtaining reliable low-frequency information with a high signal-to-noise ratio from sub-2.0 Hz field data remains a significant challenge. As a result, these low frequencies generally are extrapolated from high-frequency active-source seismic data (Li & Demanet 2016). In contrast, oceanic ambient seismic energy is inherently rich in low frequencies (0.05–2.0 Hz) (Longuet-Higgins 1950; Webb 1998; Bromirski et al. 2005), which are difficult to generate with active seismic sources. These low-frequency components potentially can complement active-source seismic data in FWI analyses within the corresponding frequency range for ocean-bottom acquisitions. However, fully exploiting ocean-bottom ambient data for low-frequency elastic model building through FWI requires a comprehensive understanding of the physical factors that influence cross-correlated wavefield observations. This necessitates interpreting the ambient wavefield data within a marine environment context characterised by acoustic and elastic media coupled at the seabed and accurately modelling these wavefields within a suitable seismic interferometry framework that accounts for various physical control factors associated with the physical system. Conventional assumptions, such as the isotropic distribution of ambient sources — commonly used to simplify cross-correlations as approximations of Green's functions — are rarely valid in marine environments. In fact, ambient seismic sources are typically more localised or azimuthally concentrated than spatially uniform (Ardhuin et al. 2015; Nakata et al. 2019). As a result, to achieve the level of accuracy required by FWI analysis, cross-correlated wavefields must be modelled as self-consistent observations rather than as simplified representations.

Recognizing these limitations, Tromp et al. (2010) introduced a framework for modelling inter-station cross-correlations that accounts for the distribution of ambient energy sources. This framework has been successfully used for inverting ambient source distributions and velocity structures in global seismology (Ermert et al. 2017; Sager et al. 2018). However, the frameworks developed at present are restricted to elastic or acoustic systems and do not encompass coupled acoustic-elastic systems with a fluid-solid interface that are prevalent in ocean-bottom seismology. This limitation renders it less effective for investigating the influence of marine physical factors on ocean-bottom sensor VSG data.

The objective of this study is twofold: (1) to outline a comprehensive framework for modelling pressure and (particle) velocity cross-correlated wavefields for dense ocean-bottom sensor arrays under different ambient source types within a coupled acoustic-elastic system; and (2) to investigate the complementary effects of key first-order physical control factors — ocean-bottom velocity structures, ambient energy source locations, ocean-bottom bathymetric depth and variations, and inhomogeneous ambient energy source distributions — on the excitation and energy partitioning of surface- and body-wave modes. OBN data potentially allow for 16 cross-component correlations derived from pressure and three-component particle velocity recordings. However, to avoid cross-correlating velocity and pressure quantities as they have different physical meanings, we only model and analyse the 3×3 particle-velocity VSG tensor and pressure-to-pressure cross-correlations, incorporating both flat and variable bathymetry with homogeneous and heterogeneous ambient source distributions. Specifically, we address the following questions: (1) How does the ambient source distribution affect surface- and body-wave excitation? (2) How does ocean-bottom depth influence the excitation and energy partitioning of these wave modes? (3) Are all cross-correlation components equally significant and, if not, which cross-correlation components best capture different wave modes? and (4) What conditions are necessary for Love-wave generation and how do inhomogeneous ambient source distributions affect their detectability? Finally, we discuss the observations made during the investigation of these control factors in the context of the broader goal of using ambient seismic wavefield energy for long-wavelength structural imaging and elastic velocity model building in seismic exploration.

2 MODELLING LOW-FREQUENCY AMBIENT VIRTUAL SHOT GATHERS FOR OCEAN-BOTTOM SENSORS

A key goal of most ambient seismic interferometry investigations is to use a cross-correlation methodology to recover accurate estimates of the Green's function between pairs of observation points. However, numerous experimental factors, such as the unavailability of favourable source types and distributions, commonly prevent VSG observations from accurately representing Green's functions. Herein, we choose not to rely on Green's function retrieval assumptions and instead interpret ambient cross correlations as self-consistent observables termed "cross-correlation functions" (CCFs). Because this approach represents a departure from standard practice, we present a comprehensive derivation of the time-domain equations for modelling CCFs between ocean-bottom receiver pairs. The CCF modelling methodology is derived from Tromp et al. (2010) and the work presented here extends this approach to modelling cross-correlation for ocean-bottom sensors located at the ocean-bottom coupled acoustic-elastic interface. We refer this framework as "cross-correlation modelling" (CCM).

A continuous CCF, denoted $\mathcal{C}_{ij}$, of two ambient wavefield recordings v_i and v_j at respective receiver locations $\boldsymbol{x}_1 = (x_1, y_1, z_1)$ and $\boldsymbol{x}_2 = (x_2, y_2, z_2)$ is explicitly given by:

$$\begin{aligned} \mathcal{C}_{ij}(\boldsymbol{x}_1, \boldsymbol{x}_2, \tau) &= \int_{-T}^{T} v_i(\boldsymbol{x}_1, t) \cdot v_j(\boldsymbol{x}_2, t+\tau)\, \mathrm{d}t \\ &= [v_i(\boldsymbol{x}_1, -t) * v_j(\boldsymbol{x}_2, t)](\tau), \end{aligned} \tag{1}$$

where $\boldsymbol{x}_1$ denotes the main receiver or virtual shot point location at which cross correlation is performed; $\boldsymbol{x}_2$ represents the VSG receiver locations; T is the selected correlation window duration; v_i and v_j are the i and j components of the particle velocity vector recorded at receivers $\boldsymbol{x}_1$ and $\boldsymbol{x}_2$; t and τ denote time and the temporal correlation lag, respectively; and $*$ represents the temporal convolution operator.

Marine ambient sources typically act either as distributed pressure sources at the ocean surface or as point force sources localised at the seafloor bathymetry (e.g., Hasselmann 1963; Nakata et al. 2019). We first derive the CCF expression for ambient pressure-type sources acting above the ocean bottom within the ocean's acoustic layer. We subsequently extend the analysis to include CCF expressions for force-type ambient sources acting below the ocean bottom within the underlying elastic solid.

Wavefield v_i excited by the ambient pressure-type source signal N, and observed at $\boldsymbol{x}$ can be expressed through the velocity Green's function (Aki & Richards 2002) as

$$v_i(\boldsymbol{x}, t) = \int \left[G_i^{v,q}(\boldsymbol{x}, \boldsymbol{\xi}, t') * N(\boldsymbol{\xi}, t')\right](t)\, \mathrm{d}\boldsymbol{\xi}, \tag{2}$$

where $G_i^{v,q}(\boldsymbol{x}, \boldsymbol{\xi}, t')$ represents the i component of observed particle velocity v at $\boldsymbol{x}$ due to an impulsive point pressure-type source q acting at spatial location $\boldsymbol{\xi}$; and $N(\boldsymbol{\xi}, t')$ denotes the ambient pressure-type source signal as a function of location $\boldsymbol{\xi}$ and time t'. Convolution of time-reversed wavefields $v_i(\boldsymbol{x}_1, -t)$ with $v_j(\boldsymbol{x}_2, t)$ results in the time-domain CCF

$$\mathcal{C}_{ij}(\boldsymbol{x}_1, \boldsymbol{x}_2) = \iint \left\{ [G_i^{v,q}(\boldsymbol{x}_1, \boldsymbol{\xi}_1) * N(\boldsymbol{\xi}_1)](-t) * \left[G_j^{v,q}(\boldsymbol{x}_2, \boldsymbol{\xi}_2) * N(\boldsymbol{\xi}_2)\right](t) \right\} \mathrm{d}\boldsymbol{\xi}_1\, \mathrm{d}\boldsymbol{\xi}_2. \tag{3}$$

Note that here and below the temporal lag τ dependence is omitted from both sides of the expression above for brevity. Rearranging the convolution in the above equation leads to

$$\mathcal{C}_{ij}(\boldsymbol{x}_1, \boldsymbol{x}_2) = \iint \left[G_j^{v,q}(\boldsymbol{x}_2, \boldsymbol{\xi}_2, t) * G_i^{v,q}(\boldsymbol{x}_1, \boldsymbol{\xi}_1, -t)\right] * [N(\boldsymbol{\xi}_1, -t) * N(\boldsymbol{\xi}_2, t)]\ \mathrm{d}\boldsymbol{\xi}_1\, \mathrm{d}\boldsymbol{\xi}_2. \tag{4}$$

Usually, traces are correlated over a selected time range for a large number of windowed subsets of the long-time recording and subsequently stacked, which effectively amounts to computing the expected value of the CCF. Therefore, we determine the ensemble-averaged CCF given by

$$\langle \mathcal{C}_{ij}(\boldsymbol{x}_1, \boldsymbol{x}_2)\rangle = \iint \left[G_j^{v,q}(\boldsymbol{x}_2, \boldsymbol{\xi}_2, t) * G_i^{v,q}(\boldsymbol{x}_1, \boldsymbol{\xi}_1, -t) \right] * \langle [N(\boldsymbol{\xi}_1, -t) * N(\boldsymbol{\xi}_2, t)] \rangle \, \mathrm{d}\boldsymbol{\xi}_1 \, \mathrm{d}\boldsymbol{\xi}_2, \tag{5}$$

where $\langle \cdot \rangle$ denotes an ensemble average. We assume that ambient sources are mutually uncorrelated (Weaver & Lobkis 2001; Snieder 2004; Shapiro et al. 2005; Wapenaar & Fokkema 2006) such that

$$\langle N(\boldsymbol{\xi}_1, -t) * N(\boldsymbol{\xi}_2, t) \rangle = S(\boldsymbol{\xi}, t)\, \delta(\boldsymbol{\xi} - \boldsymbol{\xi}_1)\, \delta(\boldsymbol{\xi} - \boldsymbol{\xi}_2), \tag{6}$$

where $\delta(\mathbf{x})$ is the Dirac delta function, and $S(\boldsymbol{\xi}, t)$ is ambient pressure-source autocorrelation function. This assumption simplifies equation 5 to

$$\langle \mathcal{C}_{ij}(\boldsymbol{x}_1, \boldsymbol{x}_2)\rangle = \int G_j^{v,q}(\boldsymbol{x}_2, \boldsymbol{\xi}, t) * [G_i^{v,q}(\boldsymbol{x}_1, \boldsymbol{\xi}, -t) * S(\boldsymbol{\xi}, t)] \, \mathrm{d}\boldsymbol{\xi}. \tag{7}$$

Using the coupled source-receiver reciprocity relation (Pandey et al. 2025),

$$G_i^{v,q}(\boldsymbol{x}_1, \boldsymbol{\xi}, t) = -G_i^{p,f}(\boldsymbol{\xi}, \boldsymbol{x}_1, t), \tag{8}$$

where $\boldsymbol{\xi}$ is above and $\boldsymbol{x}_1$ is below the ocean bottom, we can rewrite equation 7 as

$$\langle \mathcal{C}_{ij}(\boldsymbol{x}_1, \boldsymbol{x}_2)\rangle = -\int G_j^{v,q}(\boldsymbol{x}_2, \boldsymbol{\xi}, t) * \left[G_i^{p,f}(\boldsymbol{\xi}, \boldsymbol{x}_1, -t) * S(\boldsymbol{\xi}, t) \right] \mathrm{d}\boldsymbol{\xi}. \tag{9}$$

For a narrow frequency band (e.g., 0.05-1.0 Hz), we partition the ambient energy source function $S(\boldsymbol{\xi}, t)$ into its spatial and temporal dependencies as

$$S(\boldsymbol{\xi}, t) = S(\boldsymbol{\xi}) S(t), \tag{10}$$

where the relative spatial distribution of ambient wavefield energy is defined such that $S(\boldsymbol{\xi}) = 0$ and $S(\boldsymbol{\xi}) = 1$ represent effective sources with zero and the highest energy at location $\boldsymbol{\xi}$, respectively; and $S(t)$ is the ambient source-time autocorrelation function. With these definitions, the CCF becomes

$$\langle \mathcal{C}_{ij}(\boldsymbol{x}_1, \boldsymbol{x}_2)\rangle = -\int G_j^{v,q}(\boldsymbol{x}_2, \boldsymbol{\xi}, t) * \left\{ \left(G_i^{p,f}(\boldsymbol{\xi}, \boldsymbol{x}_1, -t) S(\boldsymbol{\xi}) \right) * S(t) \right\} \mathrm{d}\boldsymbol{\xi}. \tag{11}$$

Comparing this result with equation 2, we can now define the driving source (Tromp et al. 2010) of the ensemble CCF $\langle \mathcal{C}_{ij} \rangle$ as

$$q(\boldsymbol{\xi}, \boldsymbol{x}_1, t) = \left(G_i^{p,f}(\boldsymbol{\xi}, \boldsymbol{x}_1, -t) S(\boldsymbol{\xi}) \right) * S(t), \tag{12}$$

where q represents the pressure-type source injection. Thus, the driving source is simply the source-energy-weighted time-reversed wavefield recorded at ambient energy locations $\boldsymbol{\xi}$ due to a source with source-time function $S(t)$ at the virtual shot point locations $\boldsymbol{x}_1$. CCFs $\langle \mathcal{C}_{ij} \rangle$ are the ensemble-averaged wavefield recorded on ocean-bottom observation locations due to driving source q.

For ambient sources acting as point forces on local bathymetry or within elastic solid, a similar expression can be written:

$$\langle \mathcal{C}_{ij}(\boldsymbol{x}_1, \boldsymbol{x}_2)\rangle = \int G^{v,f}_{j,n}(\boldsymbol{x}_2, \boldsymbol{\xi}, t) * \left\{ \left(G^{v,f}_{n,i}(\boldsymbol{\xi}, \boldsymbol{x}_1, -t) S(\boldsymbol{\xi}) \right) * S(t) \right\} \, \mathrm{d}\boldsymbol{\xi}. \tag{13}$$

Note that in all instances of repeated subscripts in this paper, the summation convention applies. This implies that the right-hand side term in the above equation must be computed for $n = 1, 2, 3$ to account for all force components when evaluating $\langle \mathcal{C}_{ij}\rangle$:

$$\begin{aligned} \langle \mathcal{C}_{ij}(\boldsymbol{x}_1, \boldsymbol{x}_2)\rangle = &\int G^{v,f}_{j,1}(\boldsymbol{x}_2, \boldsymbol{\xi}, t) * \left\{ \left(G^{v,f}_{1,i}(\boldsymbol{\xi}, \boldsymbol{x}_1, -t) S(\boldsymbol{\xi}) \right) * S(t) \right\} \, \mathrm{d}\boldsymbol{\xi} \\ &+ \int G^{v,f}_{j,2}(\boldsymbol{x}_2, \boldsymbol{\xi}, t) * \left\{ \left(G^{v,f}_{2,i}(\boldsymbol{\xi}, \boldsymbol{x}_1, -t) S(\boldsymbol{\xi}) \right) * S(t) \right\} \, \mathrm{d}\boldsymbol{\xi} \\ &+ \int G^{v,f}_{j,3}(\boldsymbol{x}_2, \boldsymbol{\xi}, t) * \left\{ \left(G^{v,f}_{3,i}(\boldsymbol{\xi}, \boldsymbol{x}_1, -t) S(\boldsymbol{\xi}) \right) * S(t) \right\} \, \mathrm{d}\boldsymbol{\xi}. \end{aligned} \tag{14}$$

For pressure CCFs, $\mathcal{C}_{pp}$, due to ambient force sources, the expression similar to equation 11 is

$$\langle \mathcal{C}_{pp}(\boldsymbol{x}_1, \boldsymbol{x}_2)\rangle = -\int G^{p,f}_{n}(\boldsymbol{x}_2, \boldsymbol{\xi}, t) * \{ (G^{v,q}_{n}(\boldsymbol{\xi}, \boldsymbol{x}_1, -t) S(\boldsymbol{\xi})) * S(t) \} \, \mathrm{d}\boldsymbol{\xi}, \tag{15}$$

and for ambient pressure sources, an expression similar to equation 13 can be written as

$$\langle \mathcal{C}_{pp}(\boldsymbol{x}_1, \boldsymbol{x}_2)\rangle = \int G^{p,q}(\boldsymbol{x}_2, \boldsymbol{\xi}, t) * \{ (G^{p,q}(\boldsymbol{\xi}, \boldsymbol{x}_1, -t) S(\boldsymbol{\xi})) * S(t) \} \, \mathrm{d}\boldsymbol{\xi}. \tag{16}$$

Equations 11 and 13-16 provide the basis for the forward modelling of all velocity and pressure CCFs for dense ocean-bottom sensor arrays for different ambient source types, locations, and configurations. When CCFs are assembled for multiple receivers relative to a main receiver acting as a virtual shot point, the resulting gather is referred to as a virtual shot gather (VSG).

2.0.1 Ambient CCFs forward modelling workflow

Modelling ensemble CCFs under the CCM framework differs from active-shot modelling in exploration seismology because it requires two passes of forward 3-D elastic wave propagation for each ambient sources component. The first pass computes the driving source (equation 12), which depends on the ambient source-energy distribution $S(\boldsymbol{\xi})$ and the ambient wavefield source-time auto-correlation function $S(t)$. The distribution $S(\boldsymbol{\xi})$ can be estimated using real data through back-projection or beamforming techniques, while $S(t)$ is a zero-phase wavelet with a duration equal to the simulation time or $2n - 1$ time steps, where n represents the number of causal time steps. The magnitude spectrum of $S(t)$ corresponds to the ensemble-averaged power spectrum of ambient sources. The second pass evaluates the ensemble CCFs $\langle \mathcal{C}_{i,j}\rangle$ (equations 11, 13, 15, 16) resulting from the driving source calculated during the first forward pass.

We model a velocity-component virtual shot gather (VSG) for receivers located beneath the seafloor with a virtual shot point located at $\boldsymbol{x}_1 = [x_1, y_1, z_1]$ and for ambient sources acting as pressure sources on the ocean surface (equation 11) using a numerically coupled acoustic-elastic wave propagation solver by performing the following steps:

(1) Characterize the spatial distribution of the ensemble-averaged ambient wavefield energy $S(\boldsymbol{\xi})$.

(2) For $i = x$, y, or z velocity component, inject a force source with the source-time function $S(t)$ in the i direction at the virtual shot point location $\boldsymbol{x}_1$.

(3) Record the pressure-component wavefield at ambient source locations $\boldsymbol{\xi}$ due to the source implemented in Step 2 (see $G_i^{p;f}(\boldsymbol{\xi}, \boldsymbol{x}_1, -t)$ in equation 11).

(4) Time-reverse the recorded pressure wavefield and scale it by the ensemble-averaged ambient wavefield energy $S(\boldsymbol{\xi})$ to generate the corresponding driving source q needed to model the ensemble CCFs.

(5) Inject explosive sources at ambient source locations $\boldsymbol{\xi}$ with the source-time function as q. Sample the velocity wavefield components (i.e., particle velocity in $j = x, y$, or z directions) at other OBN locations $\boldsymbol{x}_2$, and multiply by -1 to compute the desired CCFs.

If using $i = z$ in Step 2 (i.e., injecting a vertical force source) and sampling the $j = z$ component of the velocity wavefield in Step 5, the modelled CCFs would correspond to a $\langle \mathcal{C}_{zz} \rangle$ auto-component velocity VSG. Similarly, if using $i = x$ in Step 2 (i.e., injecting a horizontal force source) and sampling the $j = y$ component of the velocity wavefield in Step 5, the modelled CCFs would correspond to a $\langle \mathcal{C}_{xy} \rangle$ cross-component VSG. The modelling equations for generating velocity CCFs due to ambient force sources (equation 13) and pressure CCFs (equations 15 and 16) are implemented through similar workflows.

3 NUMERICAL EXPERIMENTS

We now simulate the low-frequency vertical-component velocity cross-correlation wavefield recorded on ocean-bottom sensors using CCM approach for different offshore Earth model scenarios. The synthetic 3-D model is 190 km $\times$ 80 km $\times$ 16.5 km ($x \times y \times z$) with a regular grid spacing of 0.4 km $\times$ 0.4 km $\times$ 0.25 km ($dx \times dy \times dz$). We begin with a flat seafloor and 1-D $v_p(z)$ and $v_s(z)$ velocity profiles beneath the ocean bottom. To study the different wave modes in the modelled cross-correlation wavefields and the associated dispersion characteristics, we use two groups of ocean-bottom velocity models: (1) a soft bottom (SB) with v_s at the seafloor being much slower than the acoustic fluid velocity v_f; and (2) a hard bottom (HB) with v_s at the seafloor slightly faster than v_f. Table 1 presents the ocean-bottom model elastic properties where the v_p, v_s and ρ are defined at the ocean bottom and increase with depth according to the listed velocity gradients. The acoustic velocity, v_f, and density, ρ_f, of the homogeneous water layer are respectively set to 1500 m/s and 1000 kg/m^3. The ambient source-

Table 1. Model parameters of the soft-bottom (SB) and hard-bottom (HB) models.

Model	Ocean-bottom P-wave velocity v_p (m/s)	Ocean-bottom S-wave velocity v_s (m/s)	Ocean-bottom Density ρ (kg/m^3)	v_p gradient below ocean bottom (km/s per km)	v_s gradient below ocean bottom (km/s per km)
SB	1800	600	2100	0.40	0.23
HB	3400	1600	2100	0.40	0.23

time autocorrelation function $S(t)$ used for simulations is a zero-phase Ricker wavelet with a 0.35 Hz central frequency. We use a free-surface top boundary with all other sides defined as absorbing boundary layers. We simulate forward wave propagation using SPECFEM3D Cartesian 4.1.0 (Komatitsch & Tromp 2002a,b; Komatitsch et al. 2023) published under the GPL3 license. The open-source software implements the 3-D spectral element method (Komatitsch et al. 2000) for wave-propagation modelling. We note throughout that: (1) only the causal part of VSGs and their associated phase velocity frequency (PVF) are plotted; (2) the relative amplitudes between VSGs are not preserved; and (3) all individual VSGs are first normalised to unity prior to PVF calculation.

3.1 Uniform ambient source distribution at different depths in ocean water layer

At frequencies below 1.0 Hz, the observed ambient wavefield energy is primarily generated by ocean waves driven by two main mechanisms: (1) a primary microseism caused by the interference of ocean waves with bottom topography; and (2) a secondary microseism generated by the interference of pairs of ocean wave trains (e.g., Longuet-Higgins 1950; Hasselmann 1963; Ardhuin & Herbers 2013). For the former the seismic source can be described as a combination of tangential and vertical forces acting on the local bathymetry, while in the latter the source is a distributed pressure field acting on the ocean surface (Nakata et al. 2019).

To investigate the excitation of different wave modes and their characteristics arising from variations in the locations of ambient wavefield energy sources, we uniformly distributed ambient pressure-type sources at each grid point at various depths within the ocean water layer. The ocean-bottom interface was held constant at 1.50 km depth, and the receivers were positioned just below the ocean bottom at 1.51 km depth at each grid point along the x-axis, forming a single line covering 100 km offset. The virtual shot point is located at one end of the array at $[x_1, y_1, z_1] = [48.00, 40.00, 1.51]$ km. Figures 1 and 2 depict the VSGs (left column) and corresponding PVF plots (right column) for the SB and HB model scenarios, respectively, with ambient energy sources at the following depths: (a-b) 0.00 km, (c-d) 0.50 km, (e-f) 1.00 km, and (g-h) 1.49 km.

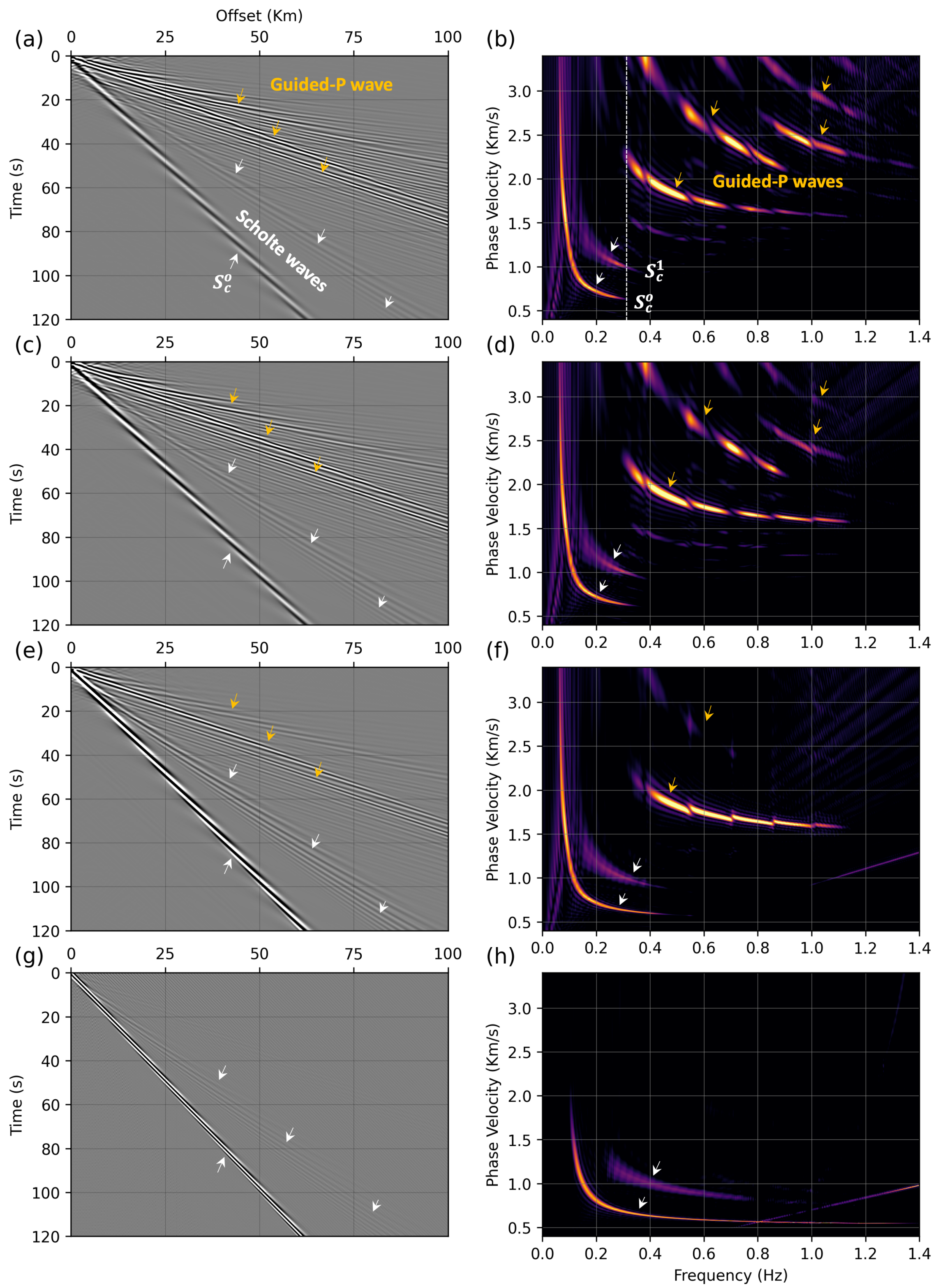

Figure 1. Vertical-component VSGs (left column) with corresponding PVFs (right column) for the SB model (see Table 1) with a constant 1.50 km water depth. Ambient energy sources are uniformly distributed at the following depths within ocean-water layer: (a-b) 0.00 km, (c-d) 0.50 km, (e-f) 1.00 km, and (g-h) 1.49 km. Scholte and guided P-wave modes are highlighted by white and yellow arrows, respectively. The vertical dotted line in (b) highlights the mode-truncation effect: the high-frequency band and the dispersive higher-mode energy of the Scholte waves are suppressed by the strong, dispersive guided P waves.

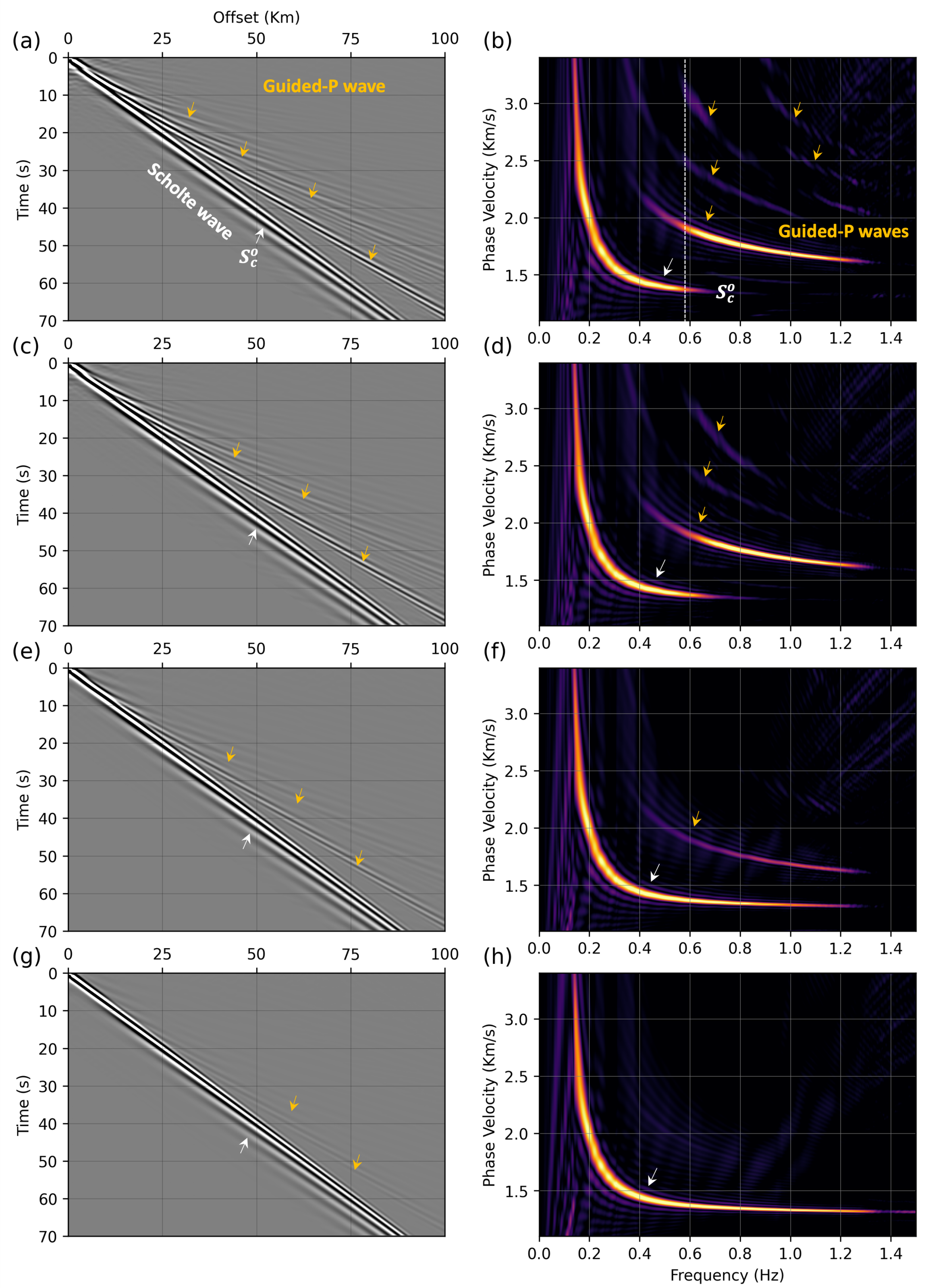

Figure 2. Vertical-component VSGs (left column) with corresponding PVFs (right column) for the HB model (see Table 1) with a constant 1.50 km water depth. Ambient energy sources are uniformly distributed at the following depths within ocean-water layer: (a-b) 0.00 km, (c-d) 0.50 km, (e-f) 1.00 km, and (g-h) 1.49 km. Scholte and guided P-wave modes are highlighted by white and yellow arrows, respectively. The vertical dotted line in (b) highlights the mode-truncation effect.

From the SB and HB cases shown respectively in Figures 1 and 2, we observe that ambient energy sources located at or near the ocean surface (Figures 1a and 2a) generate the strongest dispersive guided P-wave amplitudes (yellow arrows) relative to dispersive surface waves (white arrows) in their corresponding panels. Guided P waves are acoustic energy that travels sub-horizontally like refracted waves in subsurface sediments and reaches the receivers after reflecting repeatedly within the water column; therefore, they are also termed refracted reflections. The number of observed guided P-wave modes in the VSGs decreases as the ambient energy sources approach the seabed. When ambient energy sources are near the seabed the guided P waves are nearly absent in the VSGs and corresponding PVF plots (Figures 1g and 2g) because of the high efficiency of source-energy conversion to surface-wave modes.

The PVF plots exhibit a clear truncation effect when guided P-wave modes are present: the high-frequency band and the high-mode dispersion energy of the Scholte wave modes are suppressed by the strong, dispersive guided P-wave modes. The truncation frequency of the Scholte waves corresponds to the low cutoff frequency of the guided P-wave mode, as indicated by the white vertical lines in Figures 1b and 2b. As guided P-wave modes decrease in number and amplitude with increasing source depth the PVFs show that the fundamental Scholte wave mode (S_c^0) and its first overtone (S_c^1) exhibit a broader frequency bandwidth due to the reduced truncation effect.

3.2 Effect of ocean-water depth on Scholte and guided P-wave excitation

To illustrate the effects of water depth on the partitioning of Scholte and guided P-wave energy, we consider the SB and HB model properties of Table 1 with constant elastic layer thickness of 15 km but with different water depths and a flat seabed configuration. The ambient energy sources are uniformly distributed as pressure-type sources over the ocean surface at each grid point and the receivers are positioned 10 m below the ocean floor. Figures 3 and 4 show the vertical-component VSGs (left column) and associated PVF plots (right column) for the SB and HB model scenarios, respectively, with ocean water depths of: (a-b) 0.25 km, (c-d) 0.75 km, and (e-f) 1.50 km, and (g-h) 2.25 km.

We observe that the guided P-wave energy (yellow arrows) becomes increasingly dominant with greater water depth, extending further into the lower-frequency range. This results in the truncation of the high-frequency end and the suppression of higher-order Scholte wave modes (white arrows), thereby narrowing the Scholte wave frequency band. Furthermore, as the water depth increases, a progressively larger portion of the source energy transitions into guided P-wave modes, leading to a significant weakening of Scholte wave modes (see Figure 3 and 4 VSGs).

As illustrated in Figures 3g and 4g for the SB and HB models, respectively, the fundamental Scholte mode, S_c^0, weakens significantly with increasing depths. The corresponding PVF panels in

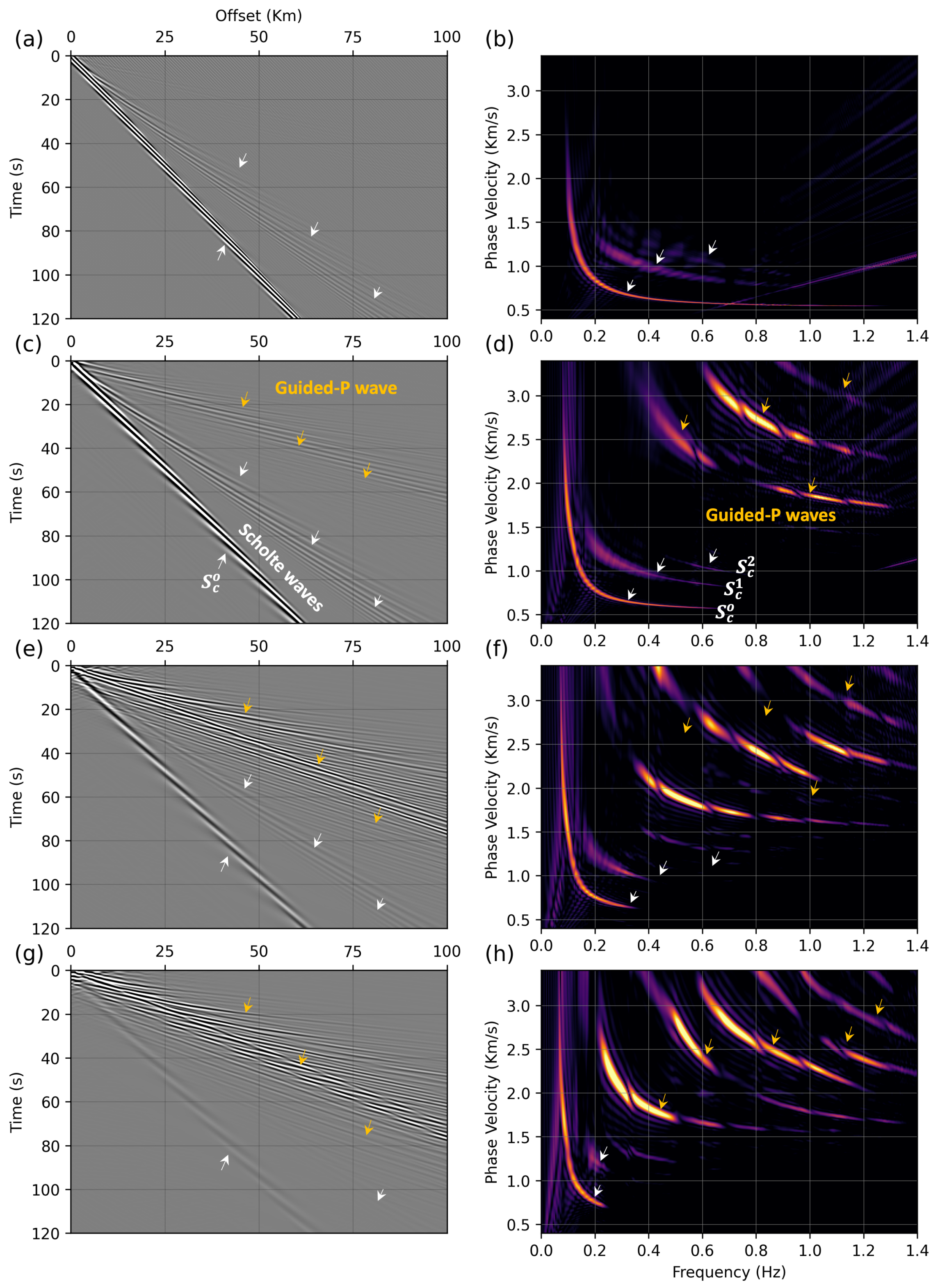

Figure 3. Vertical-component VSGs (left column) with corresponding PVFs (right column) for the SB model (see Table 1) with water depths of: (a-b) 0.25 km, (c-d) 0.75 km, and (e-f) 1.50 km, and (g-h) 2.25 km. Scholte and guided P-wave modes are highlighted by white and yellow arrows, respectively.

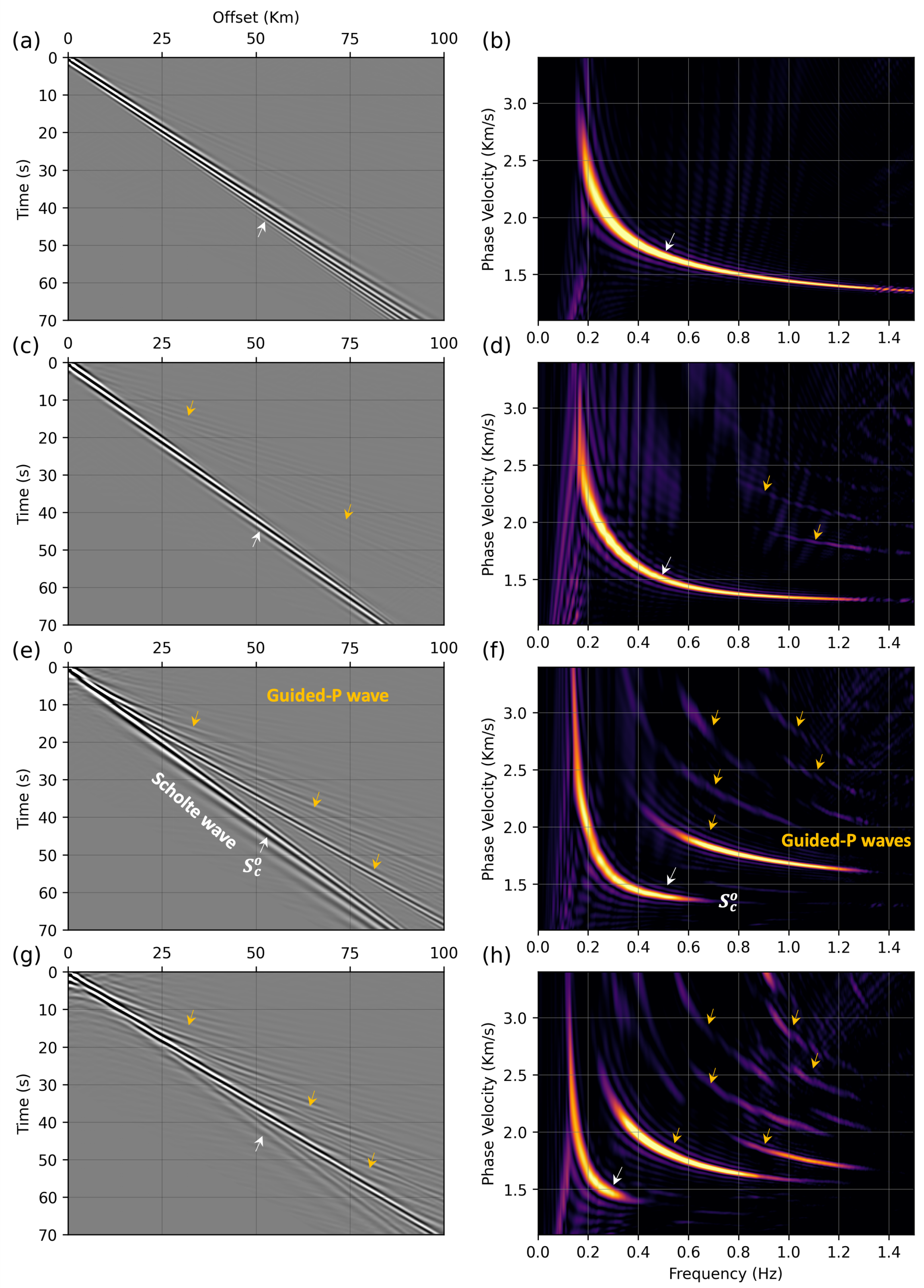

Figure 4. Vertical-component VSGs (left column) with corresponding PVFs (right column) for the HB model (see Table 1) with water depths of: (a-b) 0.25 km, (c-d) 0.75 km, and (e-f) 1.50 km, and (g-h) 2.25 km. Scholte and guided P-wave modes are highlighted by white and yellow arrows, respectively.

Figures 3h and 4h show that this mode exhibits a much narrower frequency bandwidth at deeper ocean bottoms. Specifically, in the SB model, the bandwidth reduces to below 0.2 Hz, while in the HB model, it falls below 0.4 Hz at a depth of 2.25 km. This narrowing contrasts with the broader bandwidth observed at shallower depths of 0.25 km as shown in Figures 3b and 4b.

The results presented in Figures 3 and 4 suggests a complex interplay between ocean-bottom depth and the source frequencies in controlling the expressions of Scholte and guided P-wave modes. Specifically, when the ocean depth d is small compared to the seismic wavelength (λ), the entire acoustic-elastic system behaves as a single elastic system, as the effect of the water layer becomes negligible at such low source frequencies. Under these conditions (i.e., $d << \lambda$), the influence of the ocean layer on seismic wave propagation can be accounted for as a load (Komatitsch & Tromp 2002b), and the Scholte wave velocities tend to approach those of the Rayleigh wave determined by the sub-bottom elastic layer properties (Abrahams et al. 2023). Guided P modes are apparently not excited in this scenario.

When the ocean depth is large compared to the seismic wavelength (i.e., $d >> \lambda$), though, this approximation no longer holds. The propagation of P waves within the water layer exerts a non-negligible effect on other wave modes. For the case of secondary microseisms, whose sources are located at the ocean surface, the P waves generated at these source locations are multiply reflected between the ocean surface and the seafloor, causing energy partitioning and truncation of Scholte wave energy, as observed in the aforementioned examples.

3.3 Cross-correlation tensor components and bathymetric effects

In the previous sections, we examined the modal content of vertical-component CCFs to illustrate the effects of bathymetry and ambient source distributions. However, horizontal-component CCFs also can provide relevant and equally valuable information not captured by vertical-component CCFs. Accordingly, we now perform simulations to model the auto- and cross-component velocity VSGs, forming a 3×3 VSG tensor and a pressure-component VSG. These simulations similarly assume uniform pressure-like sources at the ocean surface with source-time function as a Ricker wavelet of 0.35 Hz central frequency, accounting for interactions between ocean gravity waves at the ocean surface in the secondary microseism frequency band. We investigate the role of variable bathymetry and 3-D Earth structure in generating different wave modes, specifically focusing on Love-wave energy.

Because it is challenging to assess the polarisation patterns of different wave modes in a Cartesian coordinate system defined by the x, y, and z components – due to the azimuthal dependence of radiation polarisation for the horizontal components – we reorient the recordings to radial (r), transverse (t), and vertical components (v) in a virtual-source-centric cylindrical coordinate system. For

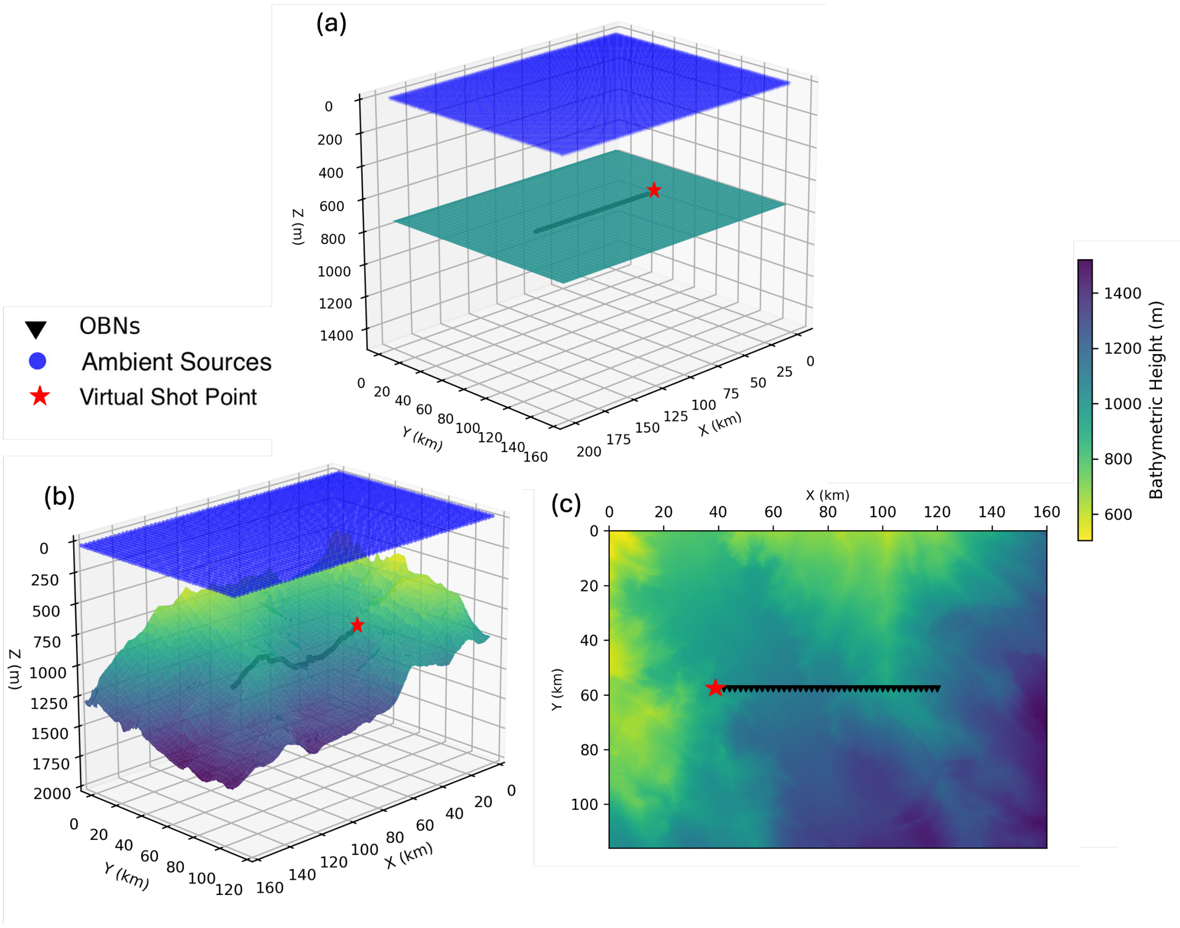

Figure 5. Secondary microseism sources, OBNs and virtual shot point location for (a) flat bathymetry, (b) variable bathymetric profile, and (c) plane view of the variable bathymetry shown in (b). The sources (blue dots) are uniformly distributed over the sea surface.

a receiver line oriented along the x-axis (see Figure 5), the x-direction becomes the radial direction, while the y-direction becomes the transverse direction. This nomenclature aligns the wave modes with the azimuth between each virtual source and receiver pair, allowing for a more natural representation of VSGs in terms of Love waves, as well as fundamental and higher-order Scholte waves.

3.3.1 Flat ocean-bottom bathymetry and 3-D Earth model with a constant vertical velocity gradient

We first model a flat seafloor at 0.75 km depth and simulate results for 3-D SB and HB Earth models with the 1-D velocity structure (i.e., a $v(z)$ velocity gradient) as detailed in Table 1. The lateral velocities do not change. Figure 5a shows the geometry of the secondary microseism sources, OBNs, and location of virtual shot point. The sources are uniformly distributed over the ocean surface. Given the flat seafloor assumption and the isotropic source distribution relative to the receiver line, the VSG tensor will be symmetric; thus, we present only the lower triangular elements of the matrix.

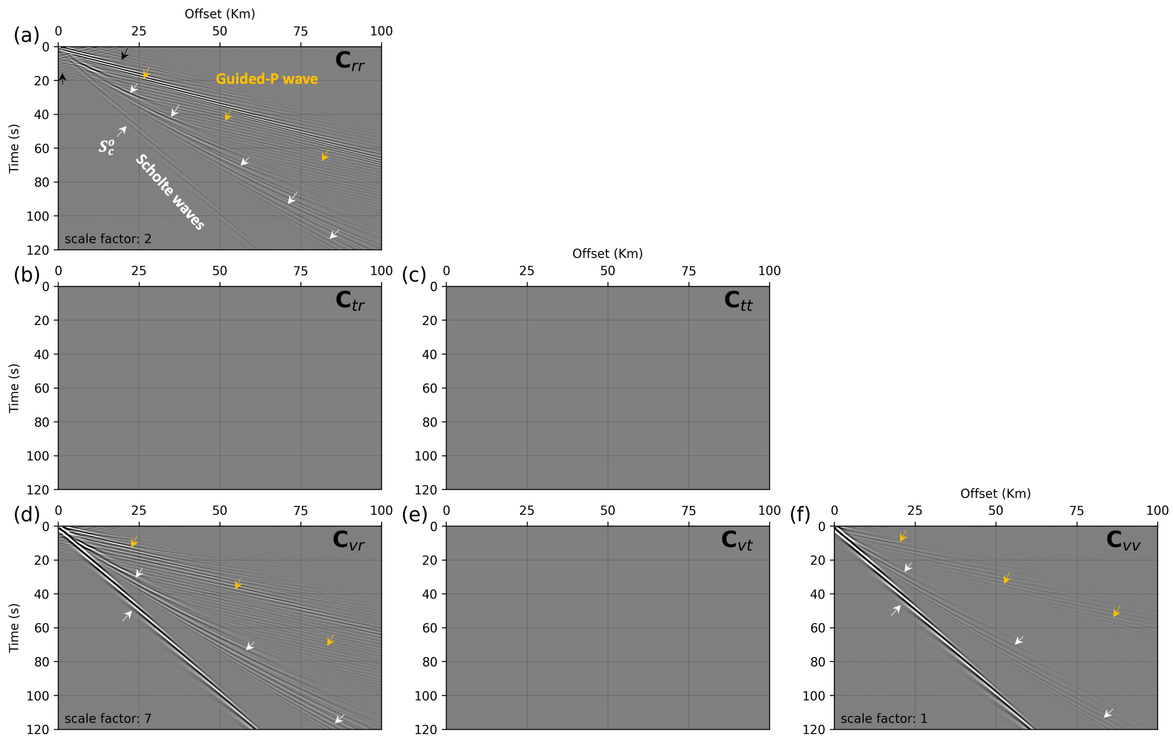

Figure 6. VSG Tensor components: (a) $\mathcal{C}_{rr}$, (b) $\mathcal{C}_{tr}$, (c) $\mathcal{C}_{tt}$, (d) $\mathcal{C}_{vr}$, (e) $\mathcal{C}_{vt}$ and (f) $\mathcal{C}_{vv}$ for the SB model (see Table 1) and a flat bathymetry with constant 0.75 km water depth. Scholte and guided P-wave modes are highlighted by white and yellow arrows, respectively. Black arrows represent intermodal cross terms. The relative amplitudes between VSGs are not preserved; however, the scaling of each panel relative to $\mathcal{C}_{vv}$ is shown at the bottom of each panel.

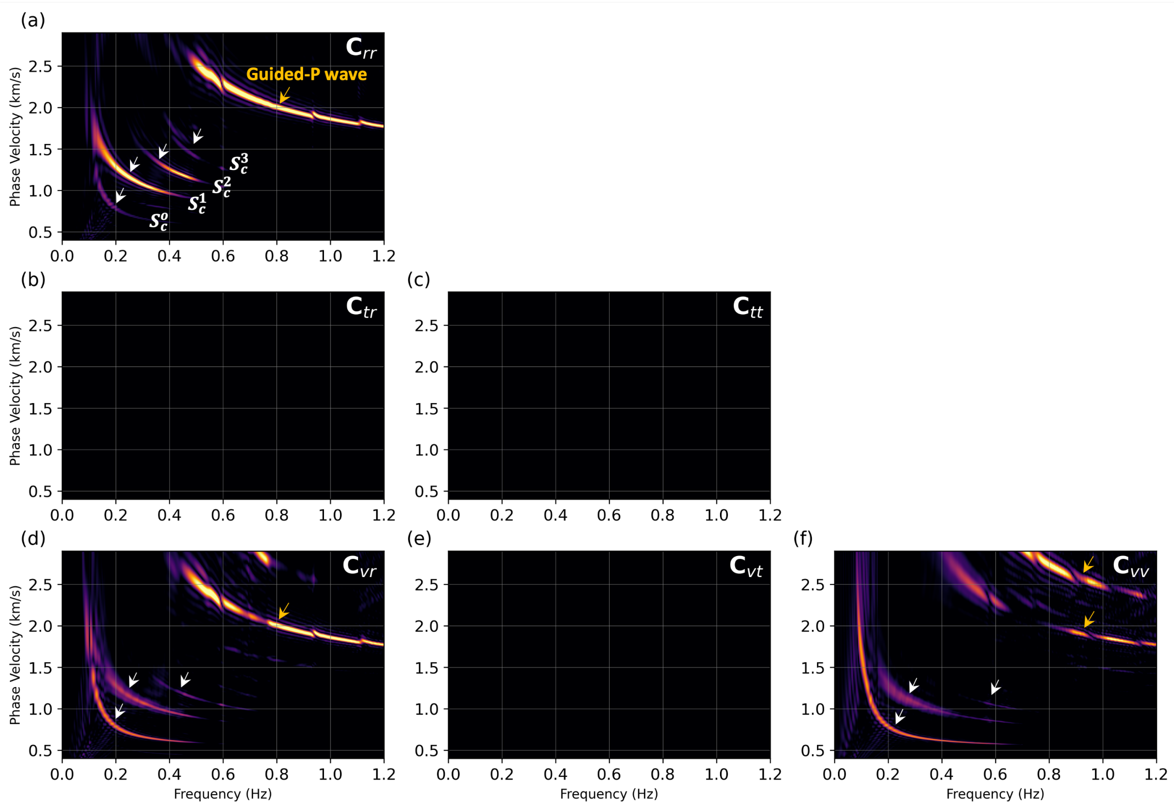

Figure 7. PVF plots for VSGs in Figure 6. (a) $\mathcal{C}_{rr}$, (b) $\mathcal{C}_{tr}$, (c) $\mathcal{C}_{tt}$, (d) $\mathcal{C}_{vr}$, (e) $\mathcal{C}_{vt}$ and (f) $\mathcal{C}_{vv}$ components. Scholte and guided P-wave modes are highlighted by white and yellow arrows, respectively.

Figure 6 shows the velocity VSG tensor components, while their corresponding PVF plots are presented in Figure 7 for the SB model scenario. The pressure component VSG and the associated PVF plot for the SB model are displayed in Figures 8a and 8b, respectively. The relative scale factor, representing the ratio of the maximum amplitudes relative to the vertical-to-vertical component VSG $\mathcal{C}_{vv}$, is noted at the bottom of each individual VSG in Figure 6.

From Figure 6 and Figure 7, the vertical-to-radial ($\mathcal{C}_{vr}$) and vertical-to-vertical ($\mathcal{C}_{vv}$) components exhibit dispersive modes of both fundamental and higher-order Scholte waves, as well as guided P-wave modes, with their lower frequencies travelling faster than higher frequencies. Due to their dispersive nature, the lower-frequency modes of these waves, characterised by longer wavelengths, penetrate deeper into the subsurface. Because the deeper layers have higher seismic velocities compared to the shallower layers, this causes the lower-frequency waves to propagate faster as they sample regions of higher velocity. Among the Scholte- and guided P-wave modes in $\mathcal{C}_{vr}$ and $\mathcal{C}_{vv}$ VSG, the fundamental-mode Scholte wave is the most dominant. At least two overtones of Scholte waves are also visible, although they appear to be weaker than the fundamental mode as indicated by their corresponding PVFs (Figures 7d and 7f).

The radial-to-radial ($\mathcal{C}_{rr}$) VSG, shown in Figure 6a, exhibits intriguing behaviour. In particular, the higher-order Scholte wave modes are more pronounced than the fundamental mode (S_c^0), with at least three overtones (S_c^1, S_c^2, S_c^3) clearly visible in the corresponding PVF plot (Figure 7a). Among the various component VSGs, the guided P-wave modes are strongest in the $\mathcal{C}_{rr}$ component relative to the Scholte modes in their respective panels. This is also evident from the $\mathcal{C}_{rr}$ PVF plot in Figure 7a when compared to the PVF plots of other components shown in Figure 7.

Because the source distribution is perfectly symmetric in the transverse direction relative to the receiver line (see Figure 5a), the guided P- and Scholte-wave energy cancels out entirely in the transverse component recordings due to summation over this isotropic source distribution. Additionally, no Love waves are observed in any of the simulated transverse component VSGs shown in Figure 6, as they are not excited in a perfectly layered and isotropic medium with an isotropic secondary microseism source distribution (Gualtieri et al. 2020), as is the case here. As a result, the VSGs and PVFs presented in Figure 6 and Figure 7 involving transverse component recordings – transverse-to-radial ($\mathcal{C}_{tr}$), transverse-to-transverse ($\mathcal{C}_{tt}$), and vertical-to-transverse ($\mathcal{C}_{vt}$) – exhibit negligible energy, with no clear transversely polarised arrivals. Notable behaviour is also observed in the pressure-to-pressure $\mathcal{C}_{pp}$ VSG,(Figure 8a) for the SB model. The fundamental and higher-order Scholte modes are visibly absent, while the guided P waves appear strong. A weak S_c^0 wave mode is discernible in the corresponding PVF in Figure 8b, though it is otherwise difficult to identify.

The black arrows in the $\mathcal{C}_{rr}$ VSG in Figure 6a highlight several intermodal cross-terms resulting

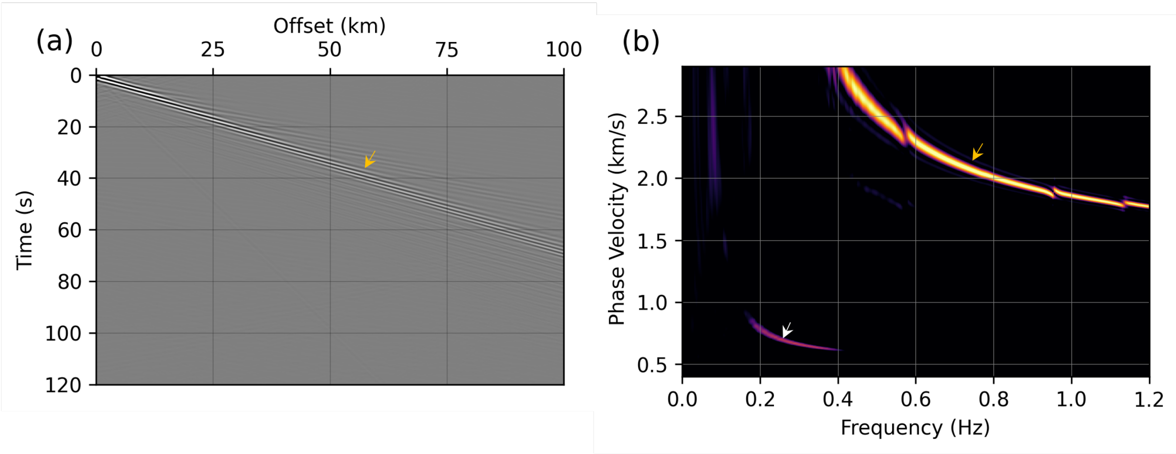

Figure 8. Pressure-to-pressure $\mathcal{C}_{pp}$ (a) VSG and (b) PVF for SB model parameters in Table 1 with constant 0.75 km bathymetry. Scholte and guided P-wave modes are highlighted by white and yellow arrows, respectively

from interactions between different wave modes. These cross-terms are less prominent in the $\mathcal{C}_{vr}$ VSG and are least evident in the $\mathcal{C}_{vv}$ VSG (Figure 6). These cross-terms arise because the P-wave modes in the horizontal component VSGs have lower energy due to partial cancellation of their contributions, caused by the isotropic source distribution. As a result, the cross-terms in the horizontal components are present with energy levels comparable to the main modes. Conversely, in the vertical component VSG, primary wave-mode energy combines constructively on the vertical-component recording, significantly weakening the cross-terms in comparison to the main modes.

Figure 9 shows the velocity VSG tensor components, while Figure 10 presents the corresponding PVF plots for the HB model scenario. Figures 11a and 11b respectively display the pressure-component VSG and the associated PVF plot for the HB model. The HB model case velocity VSGs in Figure 9 and corresponding PVFs in Figure 10 show similar behaviour to that observed in the SB model case, except for the lack of higher-order Scholte wave modes that were present in the SB case. The $\mathcal{C}_{pp}$ VSG (Figure 11a) also shows the presence of Scholte waves, as opposed to their notable absence in $\mathcal{C}_{pp}$ VSG in SB case (Figure 8a). Scholte-wave velocities are significantly faster ($>$1.4 km/s) compared to the SB case, due to the hard ocean bottom in the HB model. The $\mathcal{C}_{vr}$, $\mathcal{C}_{vv}$, and $\mathcal{C}_{rr}$ components show dispersive fundamental Scholte and guided P-wave modes. No Scholte-wave overtones are present, as evident in the PVFs presented in Figure 10. Guided P-wave modes are most pronounced in the $\mathcal{C}_{rr}$ VSG, with black arrows highlighting the cross-mode events.

3.3.2 3-D model with variable bathymetry and varying vertical and horizontal velocity gradients

We next assess the impact of variable bathymetry and 3-D velocity structure on ocean-bottom cross correlations, with a particular focus on generating and recording of Love waves due to secondary

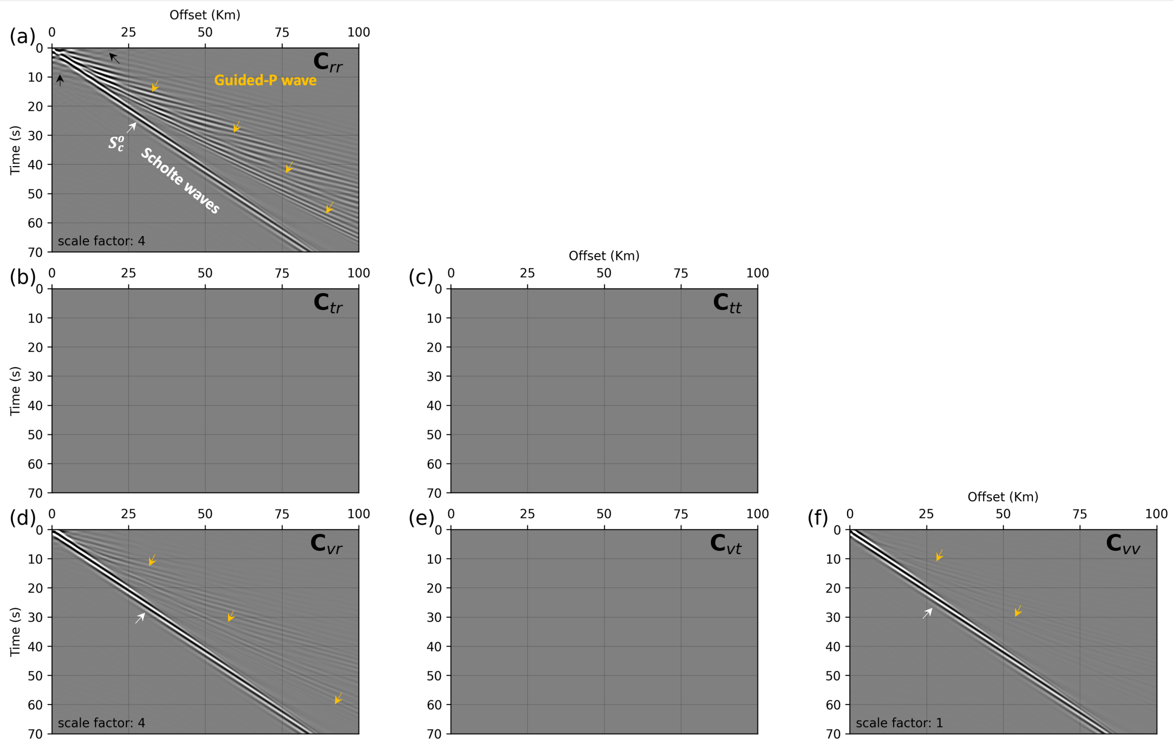

Figure 9. VSG Tensor components: (a) $\mathcal{C}_{rr}$, (b) $\mathcal{C}_{tr}$, (c) $\mathcal{C}_{tt}$, (d) $\mathcal{C}_{vr}$, (e) $\mathcal{C}_{vt}$ and (f) $\mathcal{C}_{vv}$ for the HB model parameters in Table 1 and a flat bathymetry with constant water depth of 0.75 km. Scholte and guided P-wave modes are highlighted by white and yellow arrows, respectively. Black arrows represent intermodal cross terms.

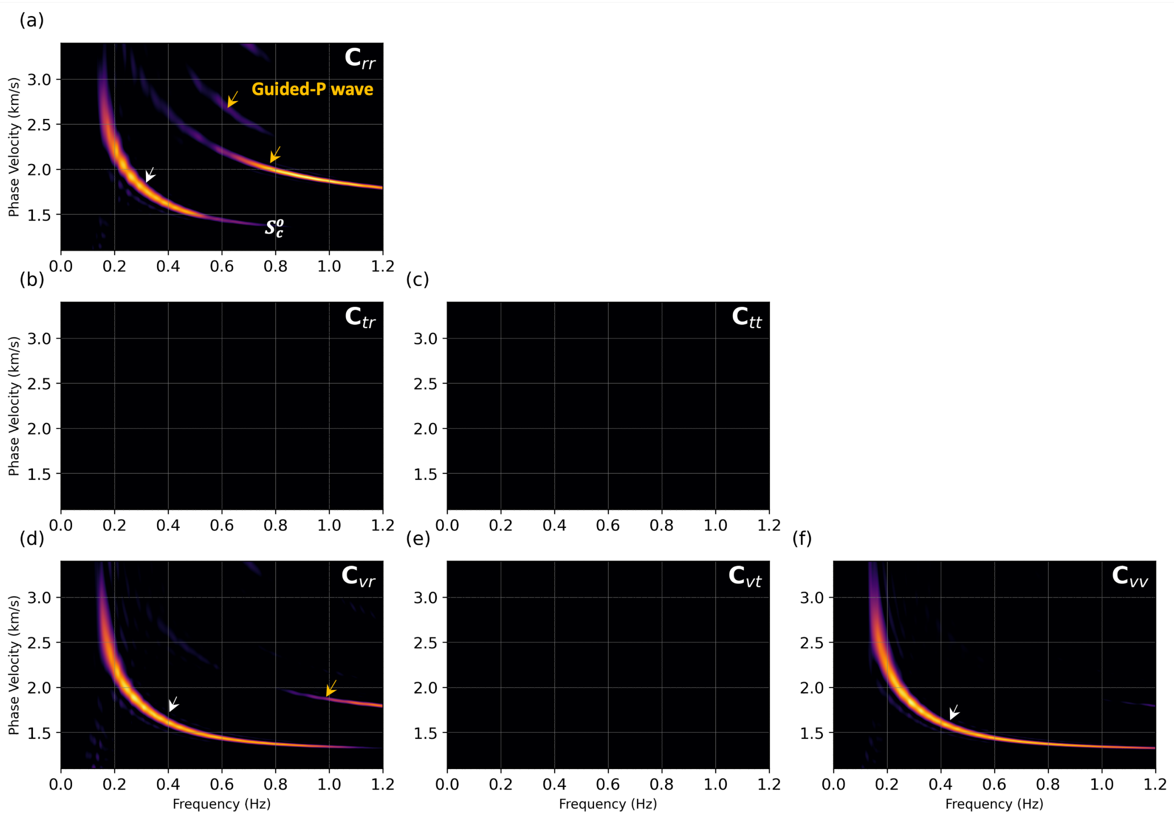

Figure 10. PVF plots for VSGs in Figure 9. (a) $\mathcal{C}_{rr}$, (b) $\mathcal{C}_{tr}$, (c) $\mathcal{C}_{tt}$, (d) $\mathcal{C}_{vr}$, (e) $\mathcal{C}_{vt}$ and (f) $\mathcal{C}_{tt}$ components. Scholte and guided P-wave modes are highlighted by white and yellow arrows, respectively.

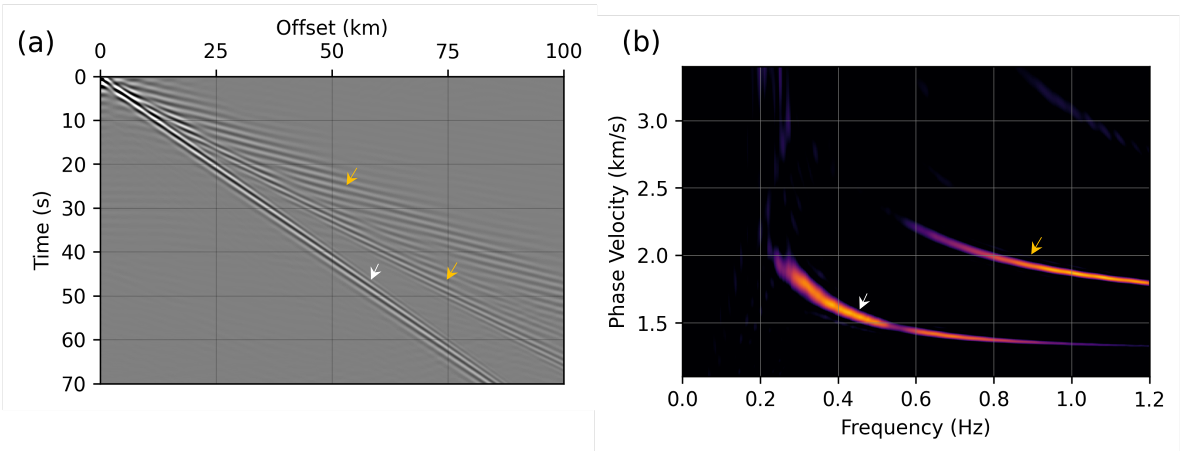

Figure 11. Pressure-to-pressure component $\mathcal{C}_{pp}$ (a) VSG and (b) PVF for HB model parameters in Table 1 and a flat bathymetry with constant water depth of 0.75 km. Scholte and guided P-wave modes are highlighted by white and yellow arrows, respectively.

microseism sources acting on the ocean surface. Primary microseisms, resulting from the direct interaction of ocean waves with the seafloor at longer periods, can generate Love waves through coupling with the seafloor (Fukao et al. 2010; Saito 2010). However, secondary microseisms, characterised by pressure-like sources acting at the ocean surface, cannot directly explain the presence of Love waves in cross correlations of horizontal-component ocean-bottom recordings.

Two main hypotheses have been proposed to account for the generation of Love waves from secondary microseism sources.The first hypothesis suggests that bathymetric variations in the source regions play a key role. Such variations can partition the vertical second-order pressure force into two components: one perpendicular to the local bathymetric slope, and being responsible for Scholte waves, the other tangent to the slope and being responsible for Love waves. The second hypothesis attributes the generation of Love waves to lateral heterogeneity within the Earth, which can cause scattering and focusing/defocusing effects (Iyer 1958; Haubrich & McCamy 1969; Gualtieri et al. 2020). Additionally, Rayleigh-to-Love wave conversion at ocean–continent boundaries may also contribute, though only a small percentage of incident Rayleigh-wave energy is converted into Love-wave energy (Gregersen & Alsop 1976). In contrast, in the absence of bathymetric variations and at low frequencies relative to ocean depth, each pressure source behaves like a vertical point force acting on a flat surface (Gualtieri et al. 2013). For a 1-D Earth model with only vertical velocity variations and flat bathymetry, as considered in the previous section, a vertical force will not generate shear motion and thus Love waves were not observed in any VSG simulation.

To incorporate these considerations, we employ velocity models that vary smoothly in both horizontal and vertical directions and include a high-resolution bathymetry profile from the northern

Gulf of Mexico. The bathymetric profile, displayed in 3-D in Figure 5b and in 2-D in Figure 5c, spans an area of 160 km $\times$ 120 km ($x \times y$). The profile has a shallowest depth of approximately 0.5 km in the northeastern corner and a deepest depth of approximately 1.5 km in the southwestern corner of the grid. This detailed bathymetric grid was generated from 3-D seismic surveys conducted in the Northern Gulf of Mexico deepwater region and is publicly available from the Bureau of Ocean Energy Management (BOEM) (`www.boem.gov/oil-gas-energy/mapping-and-data/map-gallery/northern-gom-deepwater-bathymetry-grid-3d-seismic`). We again consider the SB and HB scenarios with the velocities and densities at the ocean bottom for the two models similarly given in Table 1.

As in previous sections, the receivers for velocity and pressure cross-correlation simulations are positioned 10 m below and 10 m above the bathymetric surface, respectively. These receivers are aligned along a single line parallel to the x-axis and span an 80 km offset. The pressure-type sources are distributed isotropically across the ocean surface (see Figures 5b and 5c). The virtual shot point is located at the nearest end of the receiver array, as indicated by the stars in Figures 5b and 5c.

Figure 12 illustrates the velocity VSG tensor components, while Figure 13 shows the corresponding PVF for the SB scenario. The pressure VSG and associated PVF plot are displayed in Figures 14a and 14b, respectively. Because the PVF tensor is now asymmetric due to bathymetric variations, even though the source distribution is isotropic, we present all of the 3 $\times$ 3 VSG tensor components and the associated PVF plots. In all VSG components shown in Figure 12, we observe dispersive fundamental and higher-order Scholte and guided P-wave modes, although with varying energy, similar to the flat bathymetry scenario. Fundamental Scholte modes are indicated by white arrows, while guided P modes are marked by yellow arrows in Figure 12a. VSGs that include transverse recording as one of their components – $\mathcal{C}_{rt}$, $\mathcal{C}_{tr}$, $\mathcal{C}_{tt}$, $\mathcal{C}_{tv}$, $\mathcal{C}_{vt}$ – exhibit significantly lower energy (with relative scale factors exceeding 100, see Figure 12) compared to VSGs with radial and vertical components – $\mathcal{C}_{rr}$, $\mathcal{C}_{rv}$, $\mathcal{C}_{vr}$, $\mathcal{C}_{vv}$. This is again due to the summation over the source distribution, which is perfectly symmetric in the transverse direction relative to the receiver line (Figure 5b). However, in the presence of variable bathymetry, this symmetry does not result in the perfect cancellation of wave-mode energy in the transverse component recordings, resulting in the presence of residual energy. Consequently, VSGs that include transverse component recordings exhibit lower energy compared to those with radial and vertical components. Higher-order Scholte modes are more prominently observed in the $\mathcal{C}_{rr}$ and $\mathcal{C}_{tt}$ components compared to the fundamental Scholte mode, as evident from the associated PVFs in Figure 13. The PVFs in Figure 13 also highlight the more complex nature of guided P modes in the variable bathymetry case compared to the flat bathymetry scenario PVFs shown in Figure 7.

As expected, we observe Love waves in VSGs with transverse component recording as other re-

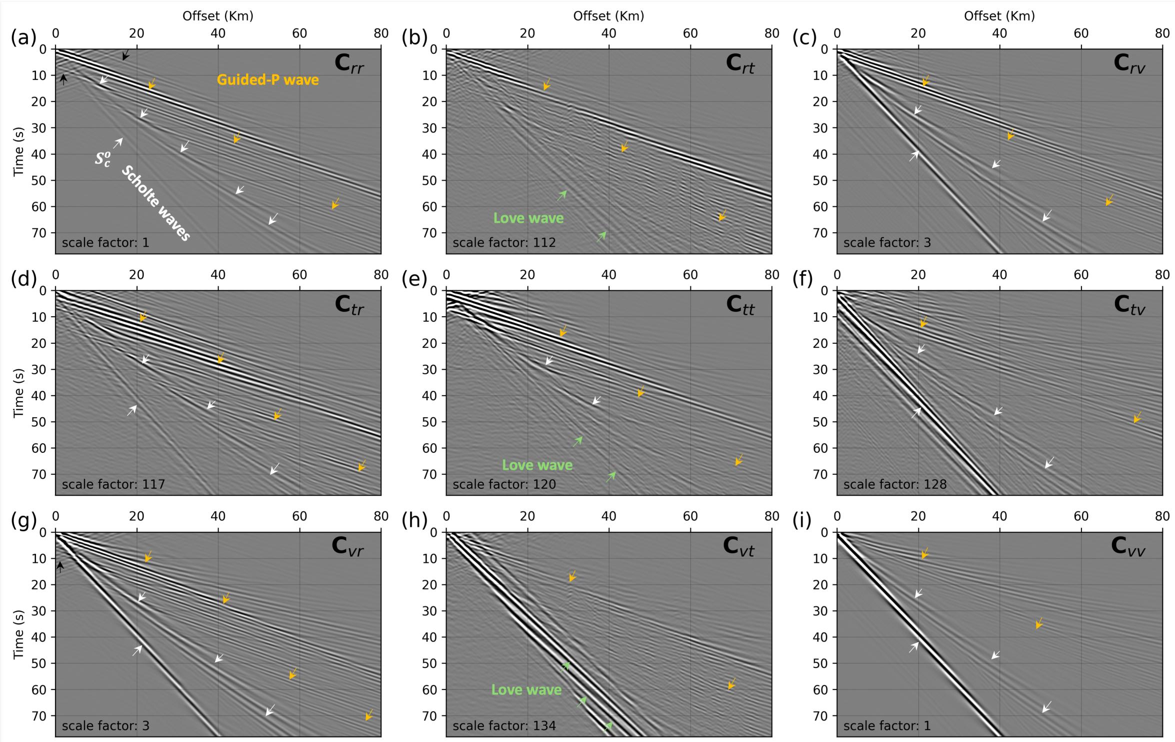

Figure 12. VSG tensor components: (a) $\mathcal{C}_{rr}$, (b) $\mathcal{C}_{rt}$, (c) $\mathcal{C}_{rv}$, (d) $\mathcal{C}_{tr}$, (e) $\mathcal{C}_{tt}$ (f) $\mathcal{C}_{tv}$, (g) $\mathcal{C}_{vr}$, (h) $\mathcal{C}_{vt}$ and (i) $\mathcal{C}_{vv}$ for the 3-D velocity structure with soft ocean bottom and variable bathymetry. Scholte and guided P-wave modes are highlighted by white and yellow arrows, respectively, while Love waves are denoted by green arrows. Black arrows represent intermodal cross terms.

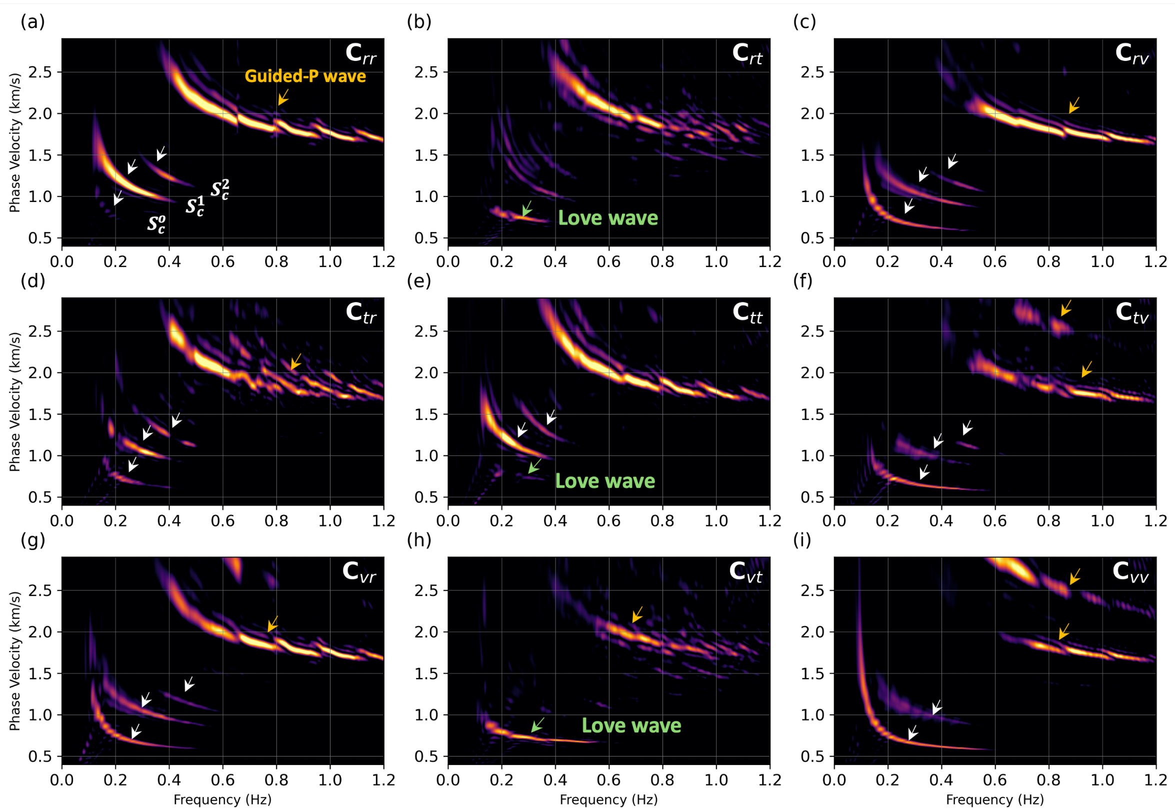

Figure 13. PVF plots for VSGs in Figure 12. (a) $\mathcal{C}_{rr}$, (b) $\mathcal{C}_{rt}$, (c) $\mathcal{C}_{rv}$, (d) $\mathcal{C}_{tr}$, (e) $\mathcal{C}_{tt}$ (f) $\mathcal{C}_{tv}$, (g) $\mathcal{C}_{vr}$, (h) $\mathcal{C}_{vt}$ and (i) $\mathcal{C}_{vv}$ components.Scholte and guided P-wave modes are highlighted by white and yellow arrows, respectively,, while Love waves are denoted by green arrows.

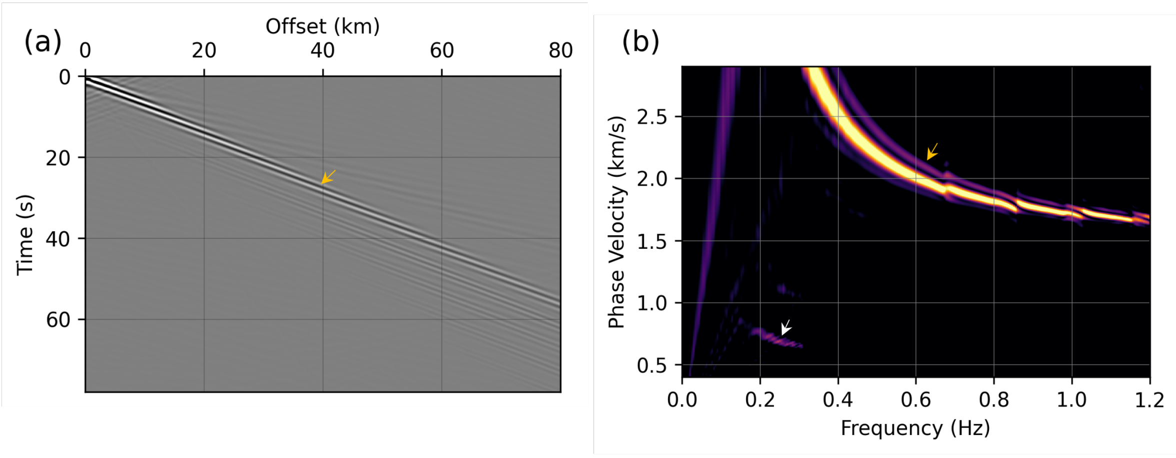

Figure 14. Pressure-to-pressure $\mathcal{C}_{pp}$ (a) VSG and (b) PVF for the 3-D velocity structure for the SB model and variable bathymetry. Scholte and guided P-wave modes are highlighted by white and yellow arrows, respectively

ceivers – $\mathcal{C}_{rt}$, $\mathcal{C}_{tt}$, and $\mathcal{C}_{vt}$. These Love waves are marked in Figures 12a ($\mathcal{C}_{rt}$ VSG), 12e ($\mathcal{C}_{tt}$ VSG), and 12h ($\mathcal{C}_{vt}$ VSG) with their most prominent appearance in the $\mathcal{C}_{vt}$ component. The $\mathcal{C}_{vt}$ component PVF plot shown in Figure 13h confirms this observation. The Love waves travel at slightly higher velocities than the fundamental Scholte waves, as evident from comparing the VSG panels of Figure 12h (containing Love waves) and Figure 12i (containing fundamental-mode Scholte waves).

The pressure VSG, $\mathcal{C}_{pp}$, shown in Figure 14a, is dominated by guided P waves. The fundamental and higher-order overtones Scholte waves are notably absent. Although very weak fundamental Scholte mode energy is present in the $\mathcal{C}_{pp}$ PVF in Figure 8b, it is otherwise difficult to identify in the associated VSG. This observation aligns with field data examples of $\mathcal{C}_{pp}$ VSG from the Mississippi Canyon area in the Gulf of Mexico, as reported in Girard et al. (2023), where the ocean bottom, as sensed by low-frequency S_c^0 waves, is soft with average near-seafloor v_s of approximately 0.5–0.6 km/s.

Figure 15 shows the velocity VSG tensor components for the HB scenario, while their corresponding PVF plots are presented in Figure 16. The pressure VSG and the associated PVF plot are displayed in Figures 17a and 17b, respectively. Similar to the observations described above for the SB case, Figure 15 reveals dispersive Scholte and guided P-wave modes, marked in Figure 15a, but no overtones of Scholte waves are present. These modes are more coherent in VSGs involving radial and vertical components – $\mathcal{C}_{rr}$, $\mathcal{C}_{rv}$, $\mathcal{C}_{vr}$, and $\mathcal{C}_{vv}$ – as indicated by the corresponding PVFs in Figure 16. In contrast, the energy in VSGs involving transverse components – $\mathcal{C}_{rt}$, $\mathcal{C}_{tr}$, $\mathcal{C}_{tt}$, $\mathcal{C}_{tv}$, and $\mathcal{C}_{vt}$ – is significantly lower (see scale factors in Figure 15). Love waves are identified in the $\mathcal{C}_{rt}$, $\mathcal{C}_{tt}$, and $\mathcal{C}_{vt}$ VSGs and in the corresponding PVFs , with their most prominent presence in the $\mathcal{C}_{vt}$ component, consistent with the SB case. However, unlike the SB model, Love waves in this case potentially exhibit multiple modes, as suggested by the PVFs in Figures 16b, 16e, and 16h.

In contrast to the SB scenario, $\mathcal{C}_{pp}$ for HB case (Figure 17a) exhibits clearly identifiable fundamental-mode Scholte wave energy. Guided P modes also are present and clearly visible in $\mathcal{C}_{pp}$ PVF plot in Figure 17b. The pressure and velocity VSGs and PVFs from this HB scenario bear a strong resemblance to those observed from the Gulf of Mexico Amendment OBN array ambient seismic data Girard et al. (2024). In that study, the ocean bottom, interpreted using low-frequency (sub-0.5 Hz) S_c^0 waves, is hard with average near-seafloor shear velocities exceeding 1.5 km/s.

The black arrows in the $\mathcal{C}_{rr}$ VSG in Figure 12a and the $\mathcal{C}_{tr}$ VSG in Figure 15d highlight several spurious cross-terms. These are present in nearly all VSGs in Figures 12 and 15, albeit with varying amplitudes and being more pronounced in some cases than in others.

3.4 Inhomogeneous ambient source distribution

The distribution of ambient source energy, as determined through data back-projection or beamforming in recent surface-wave studies, reveals that ambient energy is typically neither isotropic nor stationary. Instead, ambient source energy distributions often exhibit significant azimuthal and temporal variations (Stehly et al. 2006; Yang & Ritzwoller 2008; Yao et al. 2009). These azimuthal source strength variations can markedly affect not only the energy of different wave modes but also their excitation, particularly for Love waves.

To illustrate this, we consider an example of an inhomogeneous secondary-microseism source distribution, with the maximum source strength oriented at a northwesterly azimuth of 135°, as shown in Figure 18a. For this case, we focus on the $\mathcal{C}_{vt}$ component VSG, as Love waves are observed most prominently on this component, as demonstrated in the previous section. We use a 3-D model with a soft bottom, variable bathymetry, and OBNs positioned 10 m below the seafloor.

Figures 18b-18d present the $\mathcal{C}_{vt}$ VSGs with relative amplitude scaling for OBN lines A, B, and C, respectively, as indicated in Figure 18a. OBN line A is oriented along the direction of maximum source strength, line B is at a 45° angle, and line C is orthogonal to the maximum source strength direction. When sources are aligned with the receiver line, as with line A, the Love waves are strongest, as shown in Figure 18b. For the receiver lines at 45° (line B) and orthogonal (line C), the Love waves are more weakly observed, as seen in Figures 18c and 18d, than when compared to line A data in Figure 18b. This occurs because, for line A, the strong sources lie within the stationary phase region (Snieder 2004) and contribute to constructive interference. In contrast, for lines B and C, the sources contribute less effectively to the stationary phase integral. The black arrows in Figures 18b, 18c, and 18d represent cross-modal terms. Note that these spurious arrivals are stronger in line C compared

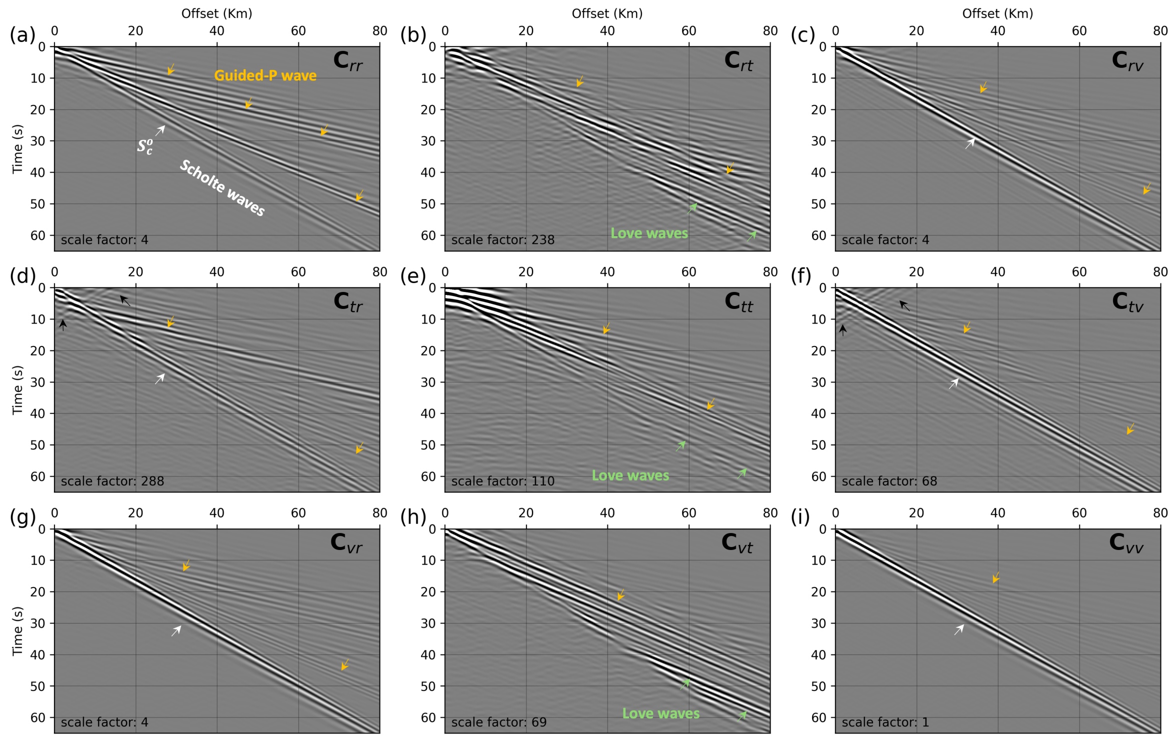

Figure 15. VSG Tensor components: (a) $\mathcal{C}_{rr}$, (b) $\mathcal{C}_{rt}$, (c) $\mathcal{C}_{rv}$, (d) $\mathcal{C}_{tr}$, (e) $\mathcal{C}_{tt}$ (f) $\mathcal{C}_{tv}$, (g) $\mathcal{C}_{vr}$, (h) $\mathcal{C}_{vt}$ and (i) $\mathcal{C}_{vv}$ for the 3-D velocity structure with hard ocean bottom and variable bathymetry. Scholte and guided P-wave modes are highlighted by white and yellow arrows, respectively, while Love waves are denoted by green arrows. Black arrows represent intermodal cross terms.

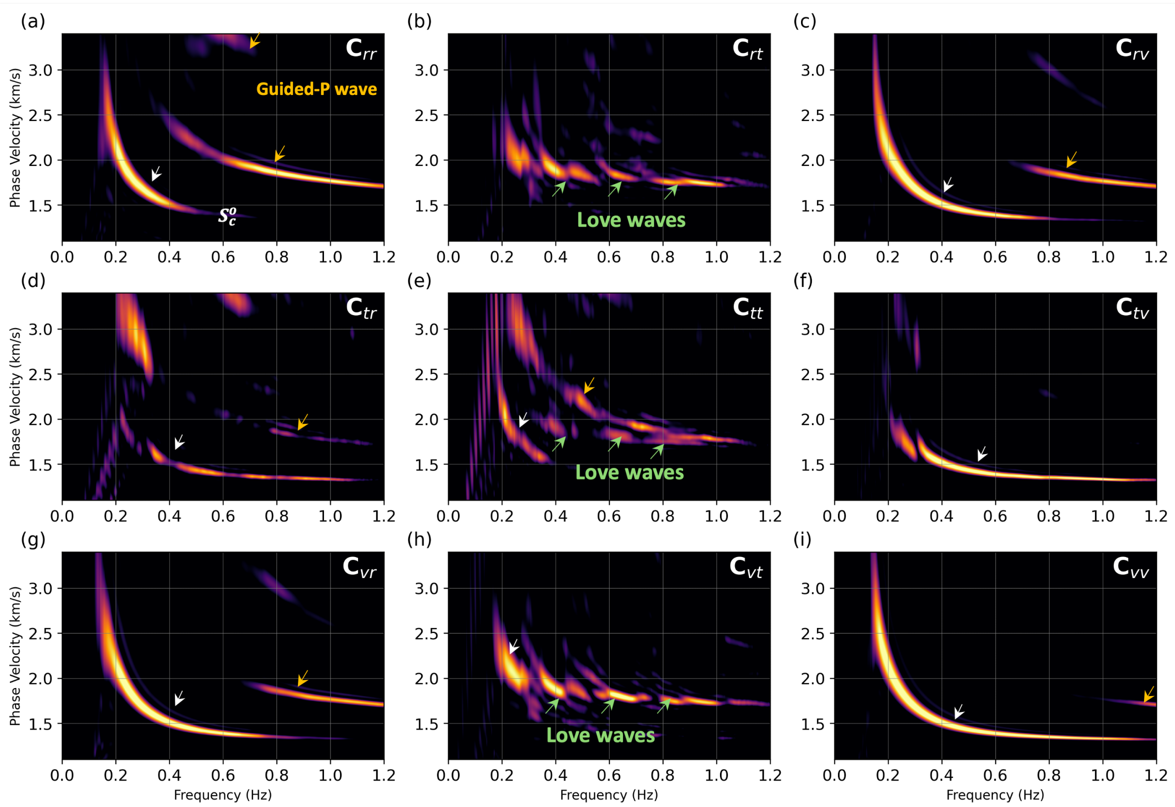

Figure 16. PVF plots for VSGs in Figure 15. (a) $\mathcal{C}_{rr}$, (b) $\mathcal{C}_{rt}$, (c) $\mathcal{C}_{rv}$, (d) $\mathcal{C}_{tr}$, (e) $\mathcal{C}_{tt}$ (f) $\mathcal{C}_{tv}$, (g) $\mathcal{C}_{vr}$, (h) $\mathcal{C}_{vt}$ and (i) $\mathcal{C}_{vv}$ components. Scholte and guided P-wave modes are highlighted by white and yellow arrows, respectively,, while Love waves are denoted by green arrows.

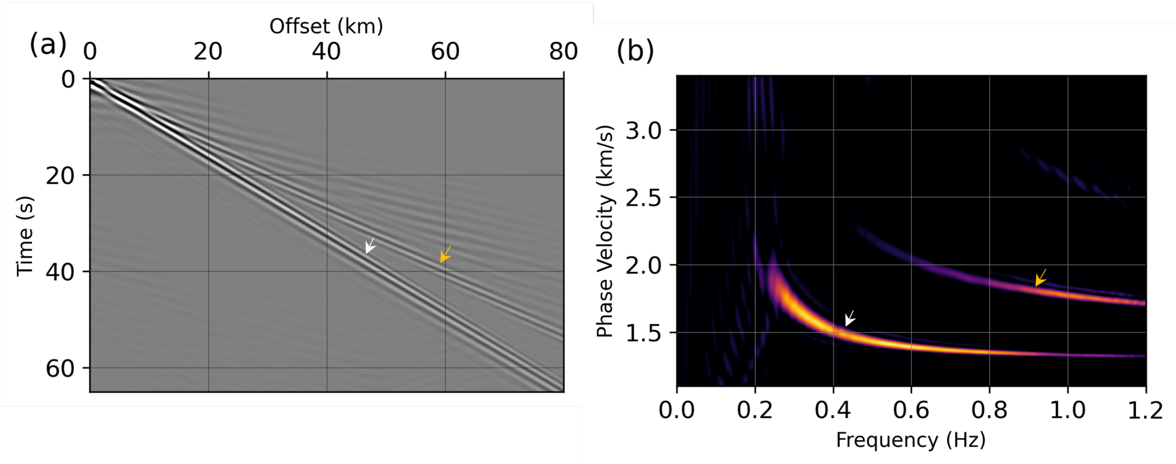

Figure 17. Pressure-to-pressure component $\mathcal{C}_{pp}$ (a) VSG and (b) PVF for the 3-D velocity structure with soft ocean bottom and variable bathymetry. Scholte and guided P-wave modes are highlighted by white and yellow arrows, respectively.

to line A due to their incomplete destructive interference, resulting from strong sources in the non-stationary phase region and their uneven distribution relative to the receiver line (Snieder et al. 2006; Halliday & Curtis 2008).

The presence of strong Love waves along the receiver line aligned with the direction of strong secondary microseism sources in this example, is consistent with the observations presented in Gualtieri

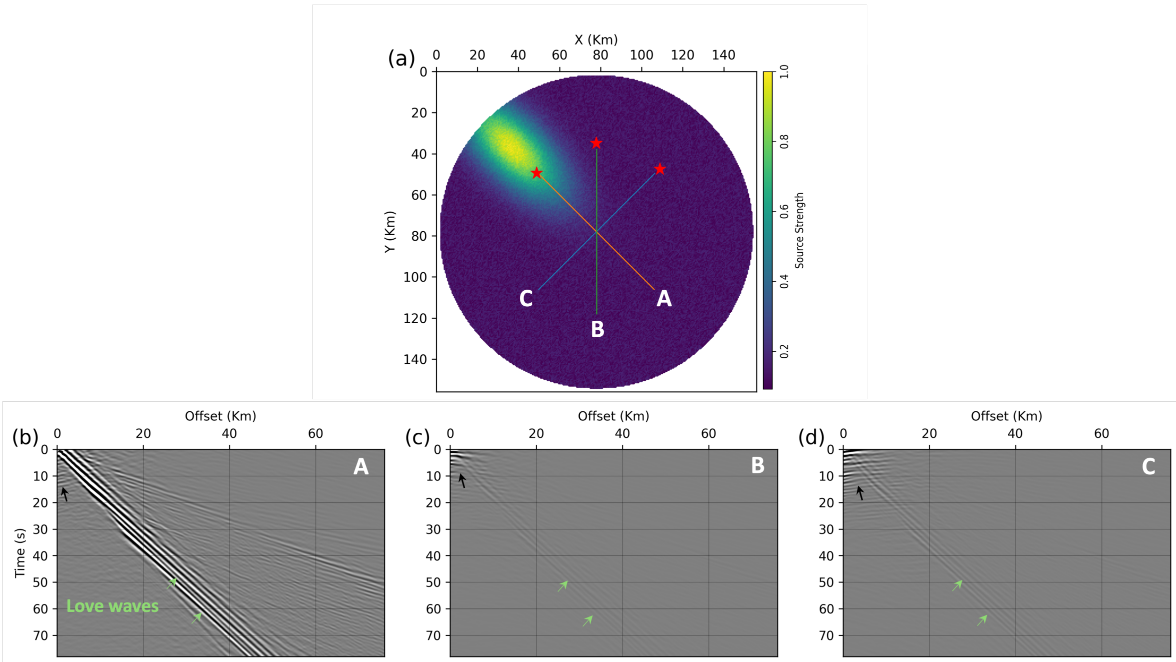

Figure 18. (a) Inhomogeneous secondary-microseism source distribution. $\mathcal{C}_{vt}$ VSG recorded on receiver line (b) A, (c) B, and (d) C, as shown in (a). The amplitudes in the VSGs are relative.

et al. (2020). One hypothesis regarding the generation of Love waves from secondary microseisms states that Love waves with significant magnitude are generated in source regions with significant pressure power spectral density, provided there are bathymetric variations in the source region. In this scenario, the observed wave direction will point toward the strongest concentration of sources. Although Love waves cannot be generated at the source itself, the conversion from Rayleigh to Love waves occurs at depth due to heterogeneous Earth structure within the same geographic region where the strongest sources are located. Therefore, when looking for the strongest Love waves in the ocean-bottom sensor cross-correlation data, it is judicious to focus on the vertical-to-traverse component VSGs $\mathcal{C}_{vt}$ in the direction of the strongest ambient sources derived through backprojection or beamforming for the low-frequency ocean-bottom sensor data.

4 DISCUSSION

We now discuss the implications of the observations made during the analysis of the controlling factors for using ambient seismic wavefields in long-wavelength structural imaging and elastic model building. A key observation concerns the impact of guided P-wave modes on Scholte-wave frequency content due to truncation effects. The ambient frequency range typically recorded on ocean-bottom sensors spans from as high as 2.0 Hz to as low as 0.01 Hz. These frequencies generally are generated by secondary microseism sources acting at the ocean surface. In shallow water where the ocean depth is much smaller than the wavelength corresponding to the source frequencies, guided P waves have a negligible effect on Scholte waves. This condition allows for broader frequency coverage and energy partitioning across the fundamental Scholte wave and higher-order modes whenever excited. In contrast, in deeper water where the wavelength is short compared to the ocean depth, P-wave propagation within the water layer significantly affects Scholte wave mode generation and the associated frequency content. Guided P waves, generated by secondary microseism sources, undergo multiple reflections between the ocean surface and the sea floor. This phenomenon leads to their dominance and the appearance of multiple modes in VSGs observations. Consequently, the Scholte-wave frequency range narrows due to high-frequency truncation, and higher-order modes are suppressed, as evidenced by the presented examples.

This phenomenon is critical for surface-wave inversion using dispersion images as well as for FWI applications. In surface-wave inversion, the modal structure and frequency bandwidth of extracted dispersion curves significantly influence both the accuracy and the maximum depth of the inversion. Incorporating higher-order modes into the inversion process can substantially enhance accuracy, improve model resolution, reduce non-uniqueness, facilitate convergence, and enable deeper subsurface investigations (Xia et al. 2003; Luo et al. 2007; Wu et al. 2020). However, the excitation of guided P waves — arising from variations in ambient source locations or bathymetry — truncates Scholte waves, thereby affecting their bandwidth and modal content. In FWI, the truncation of the higher-frequency end of Scholte wave spectra by guided P waves could result in reduced resolution due to the loss of higher frequency surface-wave data, particularly in shallow areas. Because guided P-wave modes travel sub-horizontally within the vicinity of the ocean-bottom interface, their inclusion alongside surface waves in inversion processes can enhance resolution in the near-ocean-bottom region.

Another key observation is that not all VSG components are equally important. While OBN data theoretically can provide 16 different VSGs derived from pressure and three velocity components for each virtual shot point, not all components yield distinct information useful for inversion. VSGs with transverse components are particularly effective for Love waves, which are most prominently observed on the $\mathcal{C}_{vt}$ VSG. The $\mathcal{C}_{rr}$ VSG records higher-order Scholte modes most prominently, while $\mathcal{C}_{vv}$ and $\mathcal{C}_{pp}$ provide comprehensive observations of fundamental Scholte mode and guided P waves. Collectively, VSGs with vertical components — $\mathcal{C}_{vr}, \mathcal{C}_{vt}, \mathcal{C}_{vv}$ — along with $\mathcal{C}_{rr}$ VSG, effectively capture all wave modes excited in OBN data by ambient sources.

5 CONCLUSIONS

We present a cross-correlation modelling (CCM) methodology for ambient seismic wavefields recorded on dense arrays of ocean-bottom sensors. This CCM approach differs from traditional ambient wavefield cross-correlation modelling, which relies on Green's function retrieval assumptions, by offering a more flexible and accurate framework. Using this method, we simulate the cross-correlation wavefields for velocity and pressure components and examine the impact of key first-order control factors within the context of ocean-bottom ambient seismology interferometric observations. These factors include the nature of the ocean bottom (i.e., soft versus hard), ambient source depth, ocean water column height, ocean-bottom bathymetric variations, and inhomogeneous ambient source distributions. We use 3-D Earth models that account for both vertical and horizontal velocity variations. These control factors influence the generation, propagation, and energy partitioning of seismic waves, particularly surface waves (Scholte and Love waves) and guided P-wave modes at sub-1.0 Hz frequencies.

In the absence of ocean-bottom bathymetric variations and with only vertical velocity gradients in the 3-D Earth model, we identify two primary dispersive wave types in VSGs: Scholte waves and guided P-waves; Love waves are typically absent. Synthetic experiments reveal distinct differences in wave signatures depending on the location of the ambient energy sources and the ocean-water depths. Notably, the presence and dominance of guided P-wave modes increase with greater water depths, affecting the energy distribution and frequency content of Scholte waves. In contrast, when considering a vertically and laterally heterogeneous 3-D Earth model with significant bathymetric variations, Love waves are clearly observed with a more prominent presence in the $\mathcal{C}_{vt}$ VSG components. By examining the 3×3 velocity VSG tensor in soft ocean bottom scenarios, we find that higher-order Scholte modes are more prominently observed in the $\mathcal{C}_{rr}$ and $\mathcal{C}_{tt}$ VSG components. No higher-order Scholte modes are observed with a hard ocean bottom. Ambient energy sources near the ocean surface, typically associated with secondary microseism sources, generate significant guided P modes when the ocean water depth exceeds the wavelength corresponding to the source frequency. In contrast, sources located near the seabed, characteristic of primary microseism sources, excite minimal guided P modes. Instead, the majority of source energy is concentrated in surface waves.

We also explore the effects of the heterogeneous distribution of secondary microseism sources in the presence of variable bathymetry and a heterogeneous Earth model on wave-mode excitation. The directional nature of the ambient source field — often characterised by azimuthal variations — strongly influences the amplitudes and characteristics of the resulting Love waves. This is particularly evident in the VSGs derived from ocean-bottom receiver lines aligned along different azimuthal orientations relative to the source distribution. Strong Love waves are observed when the receiver lines align with the strongest source azimuthal orientation, supporting the hypothesis that Love waves are strongly generated in the source region through Rayleigh-to-Love wave conversion, especially in the presence of ocean-bottom bathymetric variations and lateral Earth structural heterogeneity.

Overall, these observations provide a deeper understanding of the complex ambient seismic wavefield in the ocean. They emphasize the importance of considering the effects of the various key control factors explored in this study when interpreting ocean-bottom ambient cross-correlation data. Ultimately, this enables the accurate modelling and inversion of low-frequency ambient data recorded on ocean-bottom sensors for low-frequency elastic velocity model building.

REFERENCES

Abrahams, L. S., Krenz, L., Dunham, E. M., Gabriel, A.-A., & Saito, T., 2023. Comparison of methods for coupled earthquake and tsunami modelling, *Geophysical Journal International*, **234**(1), 404–426.

Aki, K. & Richards, P. G., 2002. *Quantitative seismology*, University Science Books, 2nd edn.

Ardhuin, F. & Herbers, T. H., 2013. Noise generation in the solid Earth, oceans and atmosphere, from nonlinear interacting surface gravity waves in finite depth, *Journal of Fluid Mechanics*, **716**, 316–348.

Ardhuin, F., Gualtieri, L., & Stutzmann, E., 2015. How ocean waves rock the Earth: Two mechanisms explain microseisms with periods 3 to 300 s, *Geophysical Research Letters*, **42**(3), 765–772.

Bromirski, P. D., Duennebier, F. K., & Stephen, R. A., 2005. Mid-ocean microseisms, *Geochemistry, Geophysics, Geosystems*, **6**(4).

Bussat, S. & Kugler, S., 2011. Offshore ambient-noise surface-wave tomography above 0.1 Hz and its applications, *The Leading Edge*, **30**(5), 514–524.

de Ridder, S. & Dellinger, J., 2011. Ambient seismic noise eikonal tomography for near-surface imaging at Valhall, *The Leading Edge*, **30**(5), 506–512.

de Ridder, S. A. L. & Biondi, B., 2013. Daily reservoir-scale subsurface monitoring using ambient seismic noise, *Geophysical Research Letters*, **40**(12), 2969–2974.

Ermert, L., Sager, K., Afanasiev, M., Boehm, C., & Fichtner, A., 2017. Ambient Seismic Source Inversion in a Heterogeneous Earth: Theory and Application to the Earth's Hum, *Journal of Geophysical Research: Solid Earth*, **122**(11), 9184–9207.

Fukao, Y., Nishida, K., & Kobayashi, N., 2010. Seafloor topography, ocean infragravity waves, and background Love and Rayleigh waves, *Journal of Geophysical Research: Solid Earth*, **115**(B4).

Girard, A. J., Shragge, J., & Olofsson, B., 2023. Low-frequency ambient ocean-bottom node surface-wave seismology: A Gulf of Mexico case history, *Geophysics*, **88**(1), B21–B32.

Girard, A. J., Shragge, J., Danilouchkine, M., Udengaard, C., & Gerritsen, S., 2024. Observations from the Seafloor: Ultra-low-frequency Ambient Ocean-Bottom Nodal Seismology at the Amendment Field, *Geophysical Journal International*, **239**(1), 17–36.

Gregersen, S. & Alsop, L., 1976. Mode conversion of Love waves at a continental margin, *Bulletin of the Seismological Society of America*, **66**(6), 1855–1872.

Gualtieri, L., Stutzmann, E., Capdeville, Y., Ardhuin, F., Schimmel, M., Mangeney, A., & Morelli, A., 2013. Modelling secondary microseismic noise by normal mode summation, *Geophysical Journal International*, **193**(3), 1732–1745.

Gualtieri, L., Bachmann, E., Simons, F. J., & Tromp, J., 2020. The origin of secondary microseism Love waves, *Proceedings of the National Academy of Sciences*, **117**(47), 29504–29511.

Halliday, D. & Curtis, A., 2008. Seismic interferometry, surface waves and source distribution, *Geophysical Journal International*, **175**(3), 1067–1087.

Hasselmann, K., 1963. A statistical analysis of the generation of microseisms, *Reviews of Geophysics*, **1**(2), 177–210.

Haubrich, R. A. & McCamy, K., 1969. Microseisms: Coastal and pelagic sources, *Reviews of Geophysics*, **7**(3), 539–571.

Iyer, H., 1958. A Study on the Direction of Arrival of Microseisms at Kew Observatory, *Geophysical Journal International*, **1**(1), 32–43.

Komatitsch, D. & Tromp, J., 2002a. Spectral-element simulations of global seismic wave propagation—I. Validation, *Geophysical Journal International*, **149**(2), 390–412.

Komatitsch, D. & Tromp, J., 2002b. Spectral-element simulations of global seismic wave propagation—II. Three-dimensional models, oceans, rotation and self-gravitation, *Geophysical Journal International*, **150**(1), 303–318.

Komatitsch, D., Barnes, C., & Tromp, J., 2000. Wave propagation near a fluid-solid interface: A spectral-element approach, *Geophysics*, **65**(2), 623–631.

Komatitsch, D., Tromp, J., Garg, R., Gharti, H. N., Nagaso, M., Oral, E., Peter, D., Afanasiev, M., Almada, R., Ampuero, J. P., Bachmann, E., Bai, K., Basini, P., Beller, S., Bishop, J., Bissey, F., Blitz, C., Bottero, A., Bozdag, E., & Zhu, H., 2023. Specfem/specfem3d: Specfem3d v4.1.0.

Li, Y. E. & Demanet, L., 2016. Full-waveform inversion with extrapolated low-frequency data, *Geophysics*, **81**(6), R339–R348.

Longuet-Higgins, M. S., 1950. A theory of the origin of microseisms, *Philosophical Transactions of the Royal Society of London. Series A, Mathematical and Physical Sciences*, **243**(857), 1–35.

Luo, Y., Xia, J., Liu, J., Liu, Q., & Xu, S., 2007. Joint inversion of high-frequency surface waves with fundamental and higher modes, *Journal of Applied Geophysics*, **62**(4), 375–384.

Mordret, A., Landès, M., Shapiro, N., Singh, S., Roux, P., & Barkved, O., 2013. Near-surface study at the Valhall oil field from ambient noise surface wave tomography, *Geophysical Journal International*, **193**(3), 1627–1643.

Nakata, N., Gualtieri, L., & Fichtner, A., 2019. *Seismic Ambient Noise*, Cambridge University Press.

Ning, I. L. C., Tan, J., & Dash, R., 2024. Sparse ocean-bottom node seismic interferometry and inversion: A Gulf of Mexico study, in *Fourth International Meeting for Applied Geoscience & Energy*, pp. 1830–1834, Society of Exploration Geophysicists and American Association of Petroleum Geologists.

Pandey, A., de Ridder, S., Shragge, J., & Girard, A. J., 2025. Ocean-bottom seismic interferometry in coupled acoustic-elastic media, Under review in Geophysical Journal International.

Sager, K., Ermert, L., Boehm, C., & Fichtner, A., 2018. Towards full waveform ambient noise inversion, *Geophysical Journal International*, **212**(1), 566–590.

Saito, T., 2010. Love-wave excitation due to the interaction between a propagating ocean wave and the sea-bottom topography, *Geophysical Journal International*, **182**(3), 1515–1523.

Shapiro, N. M., Campillo, M., Stehly, L., & Ritzwoller, M. H., 2005. High-Resolution Surface-Wave Tomography from Ambient Seismic Noise, *Science*, **307**(5715), 1615–1618.

Snieder, R., 2004. Extracting the Green's function from the correlation of coda waves: A derivation based on stationary phase, *Physical Review E*, **69**(4), 046610.

Snieder, R., Wapenaar, K., & Larner, K., 2006. Spurious multiples in seismic interferometry of primaries, *Geophysics*, **71**(4), SI111–SI124.

Stehly, L., Campillo, M., & Shapiro, N., 2006. A study of the seismic noise from its long-range correlation properties, *Journal of Geophysical Research: Solid Earth*, **111**(B10).

Stewart, P., 2006. Interferometric imaging of ocean bottom noise, in *SEG International Exposition and Annual Meeting*, SEG.

Tromp, J., Luo, Y., Hanasoge, S., & Peter, D., 2010. Noise cross-correlation sensitivity kernels, *Geophysical Journal International*, **183**(2), 791–819.

Virieux, J. & Operto, S., 2009. An overview of full-waveform inversion in exploration geophysics, *Geophysics*, **74**(6), WCC1–WCC26.

Wapenaar, K. & Fokkema, J., 2006. Green's function representations for seismic interferometry, *Geophysics*, **71**(4), SI33–SI46.

Weaver, R. L. & Lobkis, O. I., 2001. Ultrasonics without a Source: Thermal Fluctuation Correlations at MHz Frequencies, *Physical Review Letters*, **87**(13), 134301.

Webb, S. C., 1998. Broadband seismology and noise under the ocean, *Reviews of Geophysics*, **36**(1), 105–142.

Wu, G. X., Pan, L., Wang, J. N., & Chen, X., 2020. Shear Velocity Inversion Using Multimodal Dispersion Curves From Ambient Seismic Noise Data of USArray Transportable Array, *Journal of Geophysical Research: Solid Earth*, **125**(1), e2019JB018213.

Xia, J., Miller, R. D., Park, C. B., & Tian, G., 2003. Inversion of high frequency surface waves with fundamental and higher modes, *Journal of Applied Geophysics*, **52**(1), 45–57.

Yang, Y. & Ritzwoller, M. H., 2008. Characteristics of ambient seismic noise as a source for surface wave tomography, *Geochemistry, Geophysics, Geosystems*, **9**(2).

Yao, H., Campman, X., de Hoop, M. V., & van der Hilst, R. D., 2009. Estimation of surface wave Green's functions from correlation of direct waves, coda waves, and ambient noise in SE Tibet, *Physics of the Earth and Planetary Interiors*, **177**(1-2), 1–11.